Enomoto *et al. Earth, Planets and Space* *(2025) 77:83*
https://doi.org/10.1186/s40623-025-02213-w

Earth, Planets and Space

EXPRESS LETTER **Open Access**

Multi-fault segment complexity and multi-rupture episodes during the 2024 Mw 7.5 Noto Peninsula earthquake

Rintaro Enomoto[1*], Yoshihiro Kaneko[1], Chi-Hsien Tang[2], Yo Fukushima[2], Hiroyuki Goto[3] and Shin'ichi Miyazaki[1]

Abstract

Major intraplate earthquakes pose a substantial threat to nearby inhabited regions, but their rupture characteristics are often unclear due to limited observations. The 2024 Mw 7.5 Noto Peninsula earthquake in Japan, recorded by numerous near-fault strong-motion seismometers, high-rate GNSS, and satellite data, presents a unique opportunity to investigate fault rupture evolution and the resulting strong ground motions in detail. Using kinematic rupture modeling, we developed a source model that reproduces SAR-based and GNSS data, as well as near-fault velocity and displacement waveforms with periods longer than 4 s. Our approach integrates 3D velocity and inelastic attenuation models for Japan, incorporating regional topography and bathymetry. To reduce the number of unknown parameters, we used an a priori fault slip model derived from SAR and GNSS data and fixed the fault geometry and final slip distribution, adjusting only the rupture timing and rise time of individual fault segments. The preferred source model reveals multiple slip episodes and intricate rupture evolution, including a backward-propagating rupture toward the mainshock hypocenter likely triggered by abrupt changes in local fault geometry. The mainshock hypocenter and subsequent rupture initiations occur in areas of increased shear stresses along the periphery of the preceding swarm activity. These subsequent ruptures propagated bilaterally along southwestern and northeastern fault segments with rupture speeds ranging from 1.4 to 2.1 km/s, slower than those of other intraplate thrust earthquakes of similar magnitude. The southwestward rupture broke large slip asperities (up to ∼ 10 m) on non-planar fault segments offshore Monzen, where the coseismic uplift was ∼ 4 m. Our results suggest that the 2024 Noto Peninsula earthquake is a remarkable example of a complex intraplate earthquake involving multi-segment rupture with multiple slip episodes, providing important insights into the physics of rupture propagation and the resulting ground motions.

Keywords 2024 Noto Peninsula earthquake, Kinematic source model, Complex rupture propagation, Ground motion, Earthquake swarm

---

*Correspondence:
Rintaro Enomoto
enomoto.rintaro.42n@st.kyoto-u.ac.jp
Full list of author information is available at the end of the article

Graphical Abstract

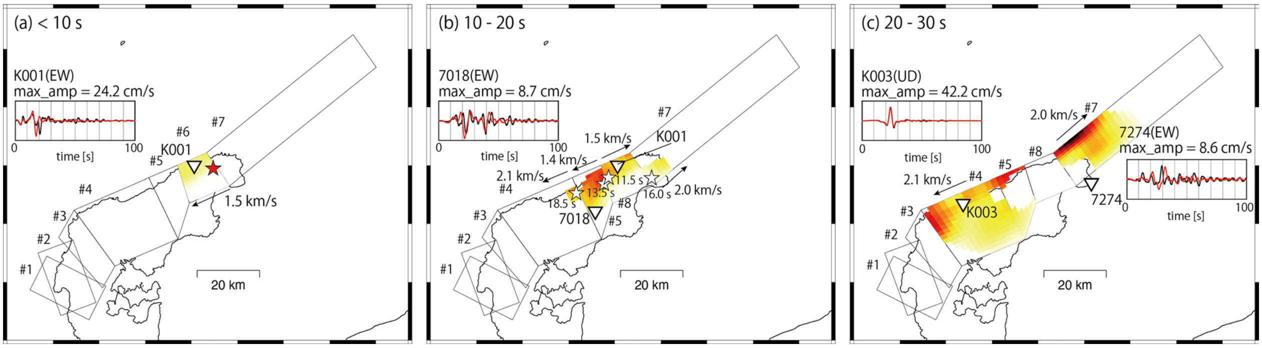

1 Introduction

On January 1st, 2024, at 7:10 UTC, a powerful earthquake with a moment magnitude (Mw) of 7.5 struck the Noto region in Ishikawa Prefecture, Japan. According to the Japan Meteorological Agency (JMA), a $M_{\mathrm{jma}}5.9$ foreshock occurred at 07:10:09.5 UTC, 13 s before the $M_{\mathrm{jma}}7.6$ mainshock at 07:10:22.5 UTC. The mainshock resulted in the tragic loss of 462 lives (including disaster-related deaths) and left 1345 individuals injured (Fire and Disaster Management Agency 2024) as of November 26th, 2024 The earthquake also triggered a tsunami with a maximum amplitude of 1.4 m (Fujii and Satake 2024) and caused up to 4 m of coastal uplift in the western part of the region (Ma et al. 2024; Masuda et al. 2024). The mainshock rupture extended approximately 160 km, from the northwestern Noto Peninsula to offshore regions in the northeast, as indicated by aftershock distribution patterns (Yoshida et al. 2024). Extensive data sets, including records from strong-motion sensors, GNSS stations, and satellite observations, were collected, offering a valuable opportunity for in-depth analysis of the rupture process during the mainshock.

Prior to the mainshock, the source region had been characterized by seismic swarm activity, as well as moderate and large earthquakes. Active faults in the Noto region, initially formed as normal faults during the Japan Sea's opening approximately 15 to 20 million years ago, now predominantly exhibit reverse faulting due to northwest–southeast compression (Okamura et al. 1995; Sato 1994). A notable earlier event was a Mw 6.7 earthquake that occurred in 2007 in the northwestern part of the Noto Peninsula (Asano and Iwata 2011; Hiramatsu et al. 2008; Kato et al. 2008, 2011; Kato and Obara 2014). Seismic activity in the epicentral region began increasing in 2018 and intensified significantly after 2020 (Amezawa et al. 2023; Yoshida et al. 2023). This increase in activity has been attributed to fluid upwelling through a shallowly dipping, permeable fault zone at a depth of ~16 km (Nishimura et al. 2023). The seismic swarm exhibited three key characteristics: ten earthquakes with Mw greater than 4.0, the formation of four seismic clusters, and diffusive hypocenter migration (Amezawa et al. 2023). In particular, the northern and eastern parts of these clusters became particularly active, with the largest earthquake of Mw 6.5 on May 5th, 2023 (Amezawa et al. 2023; Yoshida et al. 2023).

Several finite-fault source models have been proposed to explain the 2024 mainshock. Shortly after the event, the USGS released a finite fault model based on the inversion of teleseismic body waves and GEONET GNSS data (https://earthquake.usgs.gov/earthquakes/eventpage/us6000m0xl/finite-fault). Using teleseismic waveforms, Okuwaki et al. (2024) applied the potency-rate density tensor inversion method, identifying a series of discrete rupture episodes on differently oriented fault segments during the mainshock. Ma et al. (2024) developed a finite-fault source model through a joint inversion of SAR-derived displacements and GNSS horizontal offsets, and a back-projection method. Their results indicated a very slow rupture speed of ~ 0.5 km/s in the epicentral region accompanied by high-frequency radiation. Similarly, Xu et al. (2024) applied back-projection and finite-fault inversion techniques, revealing notable complexity during the initial stages of rupture. Their analysis identified two distinct rupture initiations separated by 16 km and ~10 s, with the secondary rupture initiating at the opposite edge of an ~ 14 m slip patch and propagating back toward the hypocenter (Xu et al. 2024). While these models provide valuable insights and fit their respective data sets well, significant discrepancies remain between the finite-fault slip models, likely due to differences in assumed fault geometry, simplified velocity structures, and inherent non-uniqueness. The performance of these models in explaining far-field vertical displacements is also unclear, as their models either include only a few GNSS sites or even exclude vertical displacements from the inversion.

To address these issues, we develop a finite-fault slip model based on a kinematic wavefield simulation approach to explain the near-fault data. This method accounts for the local 3D velocity structure, as well as topography and bathymetry. Our source model integrates strong-motion, GNSS, and SAR imagery data. In addition, we incorporate near-fault strong-motion records that were not used in previous studies, offering a more comprehensive understanding of the earthquake's rupture evolution.

2 Methods

To develop a kinematic source model that can reproduce dominant signals observed in near-field waveform data, we compute synthetic seismograms using the open-source seismic wave propagation software SPECFEM3D (Peter et al. 2011). Our approach employs 3D velocity and attenuation models of the relevant region (Koketsu et al. 2012) (Fig. S1), incorporating both topography and bathymetry. Sea water is not included in the computational mesh. We adopt a finite-fault approach (e.g., Hjörleifsdóttir et al. 2009; Holden et al. 2017), representing the spatiotemporal evolution of slip during the Noto Peninsula earthquake using a series of point sources. The model domain spans from 36.0° N to 38.0° N, 135.5° E to 139.0° E, with a depth range extending from the Earth's surface to 400 km. The average spacing between the computational nodes is approximately 1.25 km on the Earth's surface and increases with depth. Absorbing boundary conditions are applied at the lateral domain boundaries to minimize artificial wave reflections.

To reduce the number of unknown variables in our source model, we use the static slip model of Fukushima et al. (2024) as a priori information, fixing both the fault geometry and final slip distribution (Fig. 1a). The static slip model is informed by SAR-based coseismic displacements and GNSS measurements from both near- and far-field regions, and it is also equally compatible with direct coastal uplift observations from post-earthquake surveys (Fig. S2). The fault geometry is based on mapped active faults (Inoue and Okamura 2010), JMA's mainshock CMT solution, and 30-day relocated aftershocks (Fig. S3), with dip angles ranging from 40° to 60°. Various dip angles of planar faults and a listric fault geometry were evaluated against the geodetic data, among which the adopted geometry yielded the smallest variance reduction [Table S3 of Fukushima et al. (2024)]. The model consists of seven planar fault segments, each discretized into sub-faults measuring ~2.0 km by 1.75 km (Fig. 1a). The static slip model identifies two major slip areas: one near the mainshock epicenter and another near the western end of the peninsula, with a maximum coseismic slip of ~10 m (Fig. 1a).

To construct a kinematic rupture model, we vary only the distributions of local rupture arrival times and rise times, while assuming the final slip distribution from the aforementioned static slip model. The local rise time (T_{rise}), measured in seconds, is assumed to be proportional to the square root of the slip (D, in meters) according to the relation $T_{\text{rise}} = C_{\text{rise}}\sqrt{D}$ (Holden et al 2017; Graves and Pitarka 2010), with the constant C_{rise} set to 1.6 unless otherwise specified. The simulations are executed on the Wisteria/BDEC-01 supercomputer at the University of Tokyo, with each run taking ~3 min using 4 GPU cores. We verify the numerical resolution using a mesh refined by a factor of 1.5 and find the resulting synthetic seismograms to be virtually identical to the original, ensuring a sufficient resolution.

We use strong-motion waveform data from the K-NET, KiK-net, and JMA networks, collecting records from 38 stations (Fig. 1a). The acceleration data, sampled at 100 Hz, are integrated to derive velocity time series, which are bandpass-filtered between 4 and 50 s. This filtering is applied, because uncertainties in the local velocity structure prevent reliable deterministic modeling of higher frequency waveforms. In addition, we incorporate unfiltered displacement data from three 1-Hz GNSS stations near the mainshock faults to further validate the source model.

3 Results

3.1 Parametric study

To quantitatively assess waveform similarity, we define the misfit χ as follows:

$$\chi = \frac{1}{3N}\sum_{n=1}^{N}\sum_{i=1}^{3}\frac{|\mathbf{d}-\mathbf{m}|^2}{|\mathbf{d}||\mathbf{m}|}, \tag{1}$$

where $\mathbf{d}$ is the observed waveform vector, $\mathbf{m}$ is the synthetic waveform vector, $|\cdot|$ denotes L_2 norm of a vector, and the summation is taken over three components and N stations (Kaneko and Goto 2022). Both observed and synthetic velocity waveforms are resampled to 1 Hz for the misfit calculation, excluding a few stations with data gaps. Unless specified otherwise, we use the first 100 s of velocity data from the origin time of the M_{jma}5.9 foreshock (07:10:09.5 UTC), which occurred 13 s before the M_{jma}7.6 mainshock (07:10:22.5 UTC). This is because the assumed final slip distribution includes contributions from the foreshock, and many waveform records in

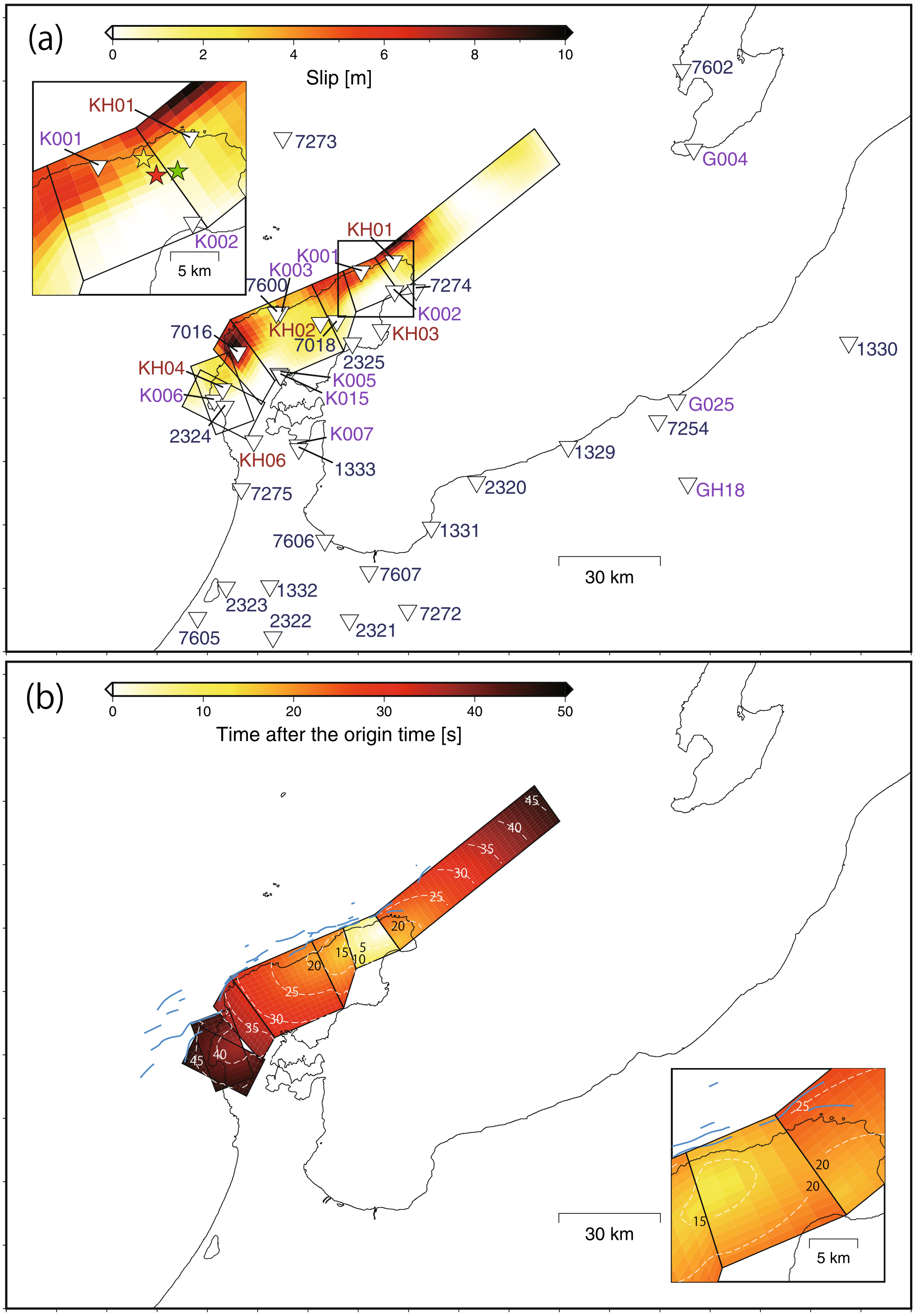

Fig. 1 **a** Slip distribution and fault geometry as determined from the inversion of geodetic data (Fukushima et al. 2024). Inverted triangles denote strong-motion stations from K-NET (purple), JMA (blue), and KiK-net (brown), labeled with the last four station digits. The yellow star marks the epicenter of the M_{jma}5.9 foreshock (07:10:09.5 UTC), the green star indicates the M_{jma}7.6 mainshock epicenter (07:10:22.5 UTC), and the red star represents the mainshock epicenter assumed in this study. Blue lines depict surface traces of known active faults. The inset zooms in on the black-outlined area. **b** Rupture arrival times (centroid times) in the best-fitting model. Contours indicate arrival times, with text labels marking fault segments. The inset details the second rupture episode on Segment #6, labeled as Segment #8 for clarity

the epicentral region contain simultaneous phase arrivals from both the foreshock and the mainshock. Note that previous finite fault models of the Noto earthquake (Ma et al. 2024; Xu et al. 2024) also assumed the foreshock origin time (±1.2 s) as the mainshock origin time (Table S1).

We first compute synthetic waveforms using the USGS finite-fault model and compare them with the observed waveforms. All the source parameters, including slip distributions and rise times, are directly taken from the USGS model. We find that the USGS model does not match the observed strong-motion data well, either in the 4–20 s period range (Fig. S4) or the 10–50 s range (Fig. S5). Significant phase misfits are evident at many stations (e.g., 7600), and the synthetic waveforms often exhibit smaller amplitudes than the observed waveforms (e.g., KH03).

Next, we test a simple source model based on the geodetically constrained slip distribution and fault geometry (Fukushima et al. 2024). Since the JMA hypocenter of the $M_{\mathrm{jma}}5.9$ foreshock (yellow star in Fig. 1a) is located at a depth of 10 km and does not lie on the assumed fault plane, we project it to the nearest point on the fault plane at a depth of 8.7 km and define this as the mainshock hypocenter (red star in Fig. 1a). We assume a spherically expanding rupture front originating from this hypocenter, with a constant rupture speed of $V_{\mathrm{r}} = 2.0$ km/s, representing quasi-uniform rupture propagation. This simplified rupture model yields an improved overall fit ($\chi = 2.363$) compared to the USGS model ($\chi = 3.299$), although the main phases in this model still arrive earlier than the observed data (Fig. S6). Furthermore, observed waveforms at some stations (e.g., K001 and 7274) in the epicentral region display two or more distinct main phase arrivals separated by several seconds, which cannot be reproduced by a single, continuous rupture episode (Fig. S6).

To develop a more accurate source model, we carefully analyze the timing of dominant phases at near-fault stations. We then adjust the location, initiation time, and rupture arrival time across all sub-faults, assuming a constant propagation speed (V_{r}) for each fault segment. The rupture initiation depths, ranging from 4 to 16 km along the lateral edges of individual fault segments, are visually evaluated to match the timing of dominant phases in the synthetic and observed waveforms at near-fault stations, identifying their optimal locations. This trial-and-error approach yields a preliminary source model that roughly matches the observed waveforms.

Following this trial-and-error approach, we employ a grid search method to identify the optimal rupture initiation times and speeds that best fit the observed waveforms (Fig. S7, S8). For a given fault segment, one parameter (e.g., $V_{\mathrm{r}1}$ or T_1) is varied while keeping the others fixed (Fig. S7). Once a new optimal combination of V_{r} and T is determined for a given fault segment, it is combined with the remaining best-fitting parameters (Fig. S7). To mitigate the effects of parameter trade-offs between fault segments, this process is iterated (indicated by the left arrow in Fig. S7) until the optimal parameters for all fault segments converge and stabilize.

The trial-and-error and grid-search procedures result in a total of 815 source scenarios, with the misfit calculated for each. The results reveal a strong dependence of misfit on V_{r} across the fault segments, indicating a high waveform sensitivity to changes in the rupture initiation time and rupture speed on individual fault segments (Fig. S8). We also examine a range of rise times by varying $C_{\mathrm{rise}} = 1.2$ to 2.4, although their influence on waveform fit is relatively minor compared to variations in rupture initiation time and V_{r}, consistent with limited resolution of local rise times inferred from a kinematic source inversion study (Ozgun Konca et al. 2013).

The best-fitting model, with a misfit of $\chi = 1.464$, demonstrates that the geodetically derived final slip model, when combined with variable rupture times, effectively reproduces local ground velocities across both the 4–20 s and 10–50 s period ranges (Fig. S9, S10). The onset, amplitude, and polarities of dominant phases are well-matched for all three components (Fig. S9). Notably, this result highlights the necessity of multiple rupture episodes on one of the fault segments (Segment #6) to explain waveforms featuring two or more distinct main phase arrivals separated by several seconds near the epicenter (Fig. 1b). Segment #6 experienced two slip episodes, followed by a subsequent rupture on the same segment, referred to as Segment #8 (Fig. 1b). For Segment #8, the model with a northeastward rupture starting at the eastern edge of Segment #8 produces a slightly smaller waveform misfit compared to one with the northeastward rupture originating from the mainshock hypocenter (Fig. S8g, h), suggesting that the second rupture episode represents a backward-propagating rupture toward the hypocenter. In the first slip episode on Segment #8, 30% of the total slip occurred, followed by 70% in the second episode, as determined by an additional grid search exploring different slip partitioning scenarios (Fig. S8i).

The parameters of the best-fitting model are summarized in Table S1, and the slip distribution with corresponding rupture timings is illustrated in Fig. 1. Below, we provide a detailed description of the rupture characteristics in this best-fitting source model.

3.2 Rupture characteristics in the best-fitting model

To illustrate the complex rupture process in the best-fitting model, snapshots of slip accumulation are presented in Fig. 2. At the origin time (T_0 =7:10:09.5 UTC), the primary rupture on a 58^o dipping fault initiated at a depth of 8.7 km, propagating southwestward along Segment #6 during the first 10 s (Fig. 2a). This initial rupture is evidenced by early wave arrivals at near-fault stations, such as K001 (Fig. 2a). The rupture progressed at a speed of 1.5 km/s, ultimately breaking the entire fault segment (#6) and accounting for 30% of the total slip on this segment, with a corresponding moment magnitude of Mw 6.4. Most of the slip was concentrated within the top 9 km of Segment #6.

Right after the initial rupture ceased in the western part of Segment #6, a secondary rupture began at a depth of ~9 km at $T_0 + 11.5$ s, propagating bilaterally (Fig. 2b). The timing of the secondary rupture initiation roughly coincides with the arrival time of the first rupture at the secondary rupture initiation point. Although the rupture start times on Segment #8 and #5 are $T_0 + 11.5$ s and $T_0 + 13.5$ s, respectively, the ~3 km separation between their initiation points suggests that the southwestward rupture front may have propagated continuously toward the initiation point on Segment #5. The southwestward rupture front extended at a speed of 1.4 km/s on Segment #5, while the backward rupture toward the hypocenter propagated at 1.5 km/s on Segment #8, as inferred from the main phases around $T_0 + 20$ s at Stations 7018 and K001 (Fig. 2a, b). This backward rupture propagation accounted for the remaining moment release (70% of slip) on Segment #6 (Fig. S8i).

At $T_0 + 16.0$ s, another significant rupture was initiated several km underneath the hypocenter at the northwestern edge of Segment #7, propagating northeastward at a speed of 2.0 km/s (Fig. 2b). The depth and timing of this rupture initiation roughly align with the JMA hypocentral depth and origin time of the $M_{\text{jma}}7.6$ mainshock (7:10:22.5 UTC), although the horizontal locations differ by ~4 km. This rupture initiated a few seconds earlier than the arrival of the back-propagating rupture at the same location. On Segment #7, the rupture broke a shallow asperity with up to ~8 m of slip and propagated northeastward, as evidenced by the main phases observed at $T_0 + 40$ s at Station 7274 (Fig. 2c).

After $T_0 + 20.0$ s, both the northeastward rupture on Segment #7 and the southwestward rupture on Segment #3 continued further propagation, resulting in a bilateral rupture pattern (Fig. 2c). The southwestward rupture propagated at speeds of 1.4 to 2.1 km/s, breaking the remaining 45^o-dipping, southern fault segments (#3, #2, and #1) in sequence, without interruption. The timing of this propagation is constrained by the large velocity pulses observed at Stations K003 and 7016, located several kilometers from the surface trace of each fault segment (Fig. 2c, d). At approximately $T_0 + 34.0$ s, the southwestward rupture ultimately reached large slip asperity (up to ~10 m) on Segment #3 offshore Monzen, where the coastal region experienced ~4 m of coseismic uplift (Fig. 2d). At approximately $T_0 + 48$ s, the southwestern rupture terminated in the vicinity of the source region of the 2007 Noto earthquake, while the northeastward rupture terminated at the northeastern end of Segment #7 in the offshore region (Fig. 2e).

The moment rate function of the best-fitting model reveals four peaks at T_0 + 7, 25, 34, and 42 s, reflecting complex rupture evolution (Fig. 2f). The first peak at $T_0 + 7$ s marks the rupture near the hypocenter (Fig. 2a). The highest peak at $T_0 + 25$ s reflects simultaneous ruptures in both the southwestern and northeastern fault segments, where relatively large slip took place (Fig. 2c). The third peak at $T_0 + 33$ s corresponds to the rupture of the largest asperity offshore Monzen (Fig. 2d). The trough in the moment rate at $T_0 + 32$ results from the absence of a significant slip patch in the northern fault segment (#7) during that time, combined with a kink in the fault geometry between Segments #3 and #4 that slightly delays the rupture progression. The fourth minor peak at $T_0 + 42$ s reflects slip on the southwestern (#1, #2) and northeastern (#7) segments (Fig. 2e).

3.3 The spatio-temporal pattern of ground motions

Ground motions of the mainshock are controlled by both the complex rupture evolution and local velocity structure. The spatio-temporal pattern of ground motions in the best-fitting source model is illustrated in

(See figure on next page.)

Fig. 2 **a**–**e** Snapshots of coseismic slip accumulation at 10-s intervals in the best-fit model. Black and red waveforms display the 4–20 s bandpass-filtered observed and synthetic waveforms, respectively, at stations marked by white inverted triangles. The red star indicates the mainshock epicenter, while white stars denote the rupture initiation points of individual fault segments. Arrows and accompanying numbers represent the along-strike direction and speed of rupture propagation for each segment. **f** Normalized moment rate function for the best-fit model. The solid red line represents the source time function for the entire fault, the dashed blue line shows the contribution from the southern segments (Segments #1–6 and #8), and the dashed blue line indicates the contribution from the northern segment (Segment #7). Time zero corresponds to the origin time assumed in this study (07:10:09.5 UTC)

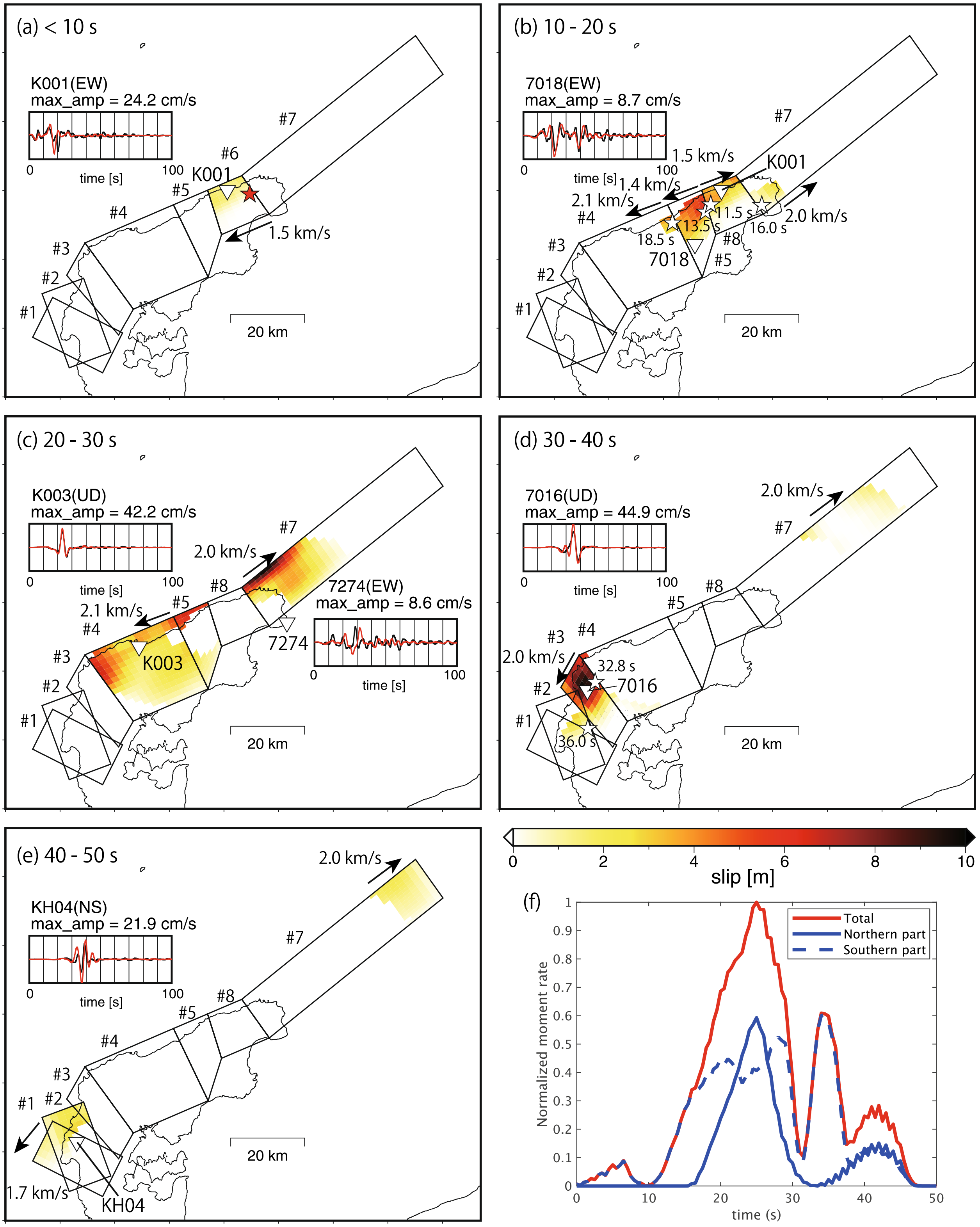

Fig. 2 (See legend on previous page.)

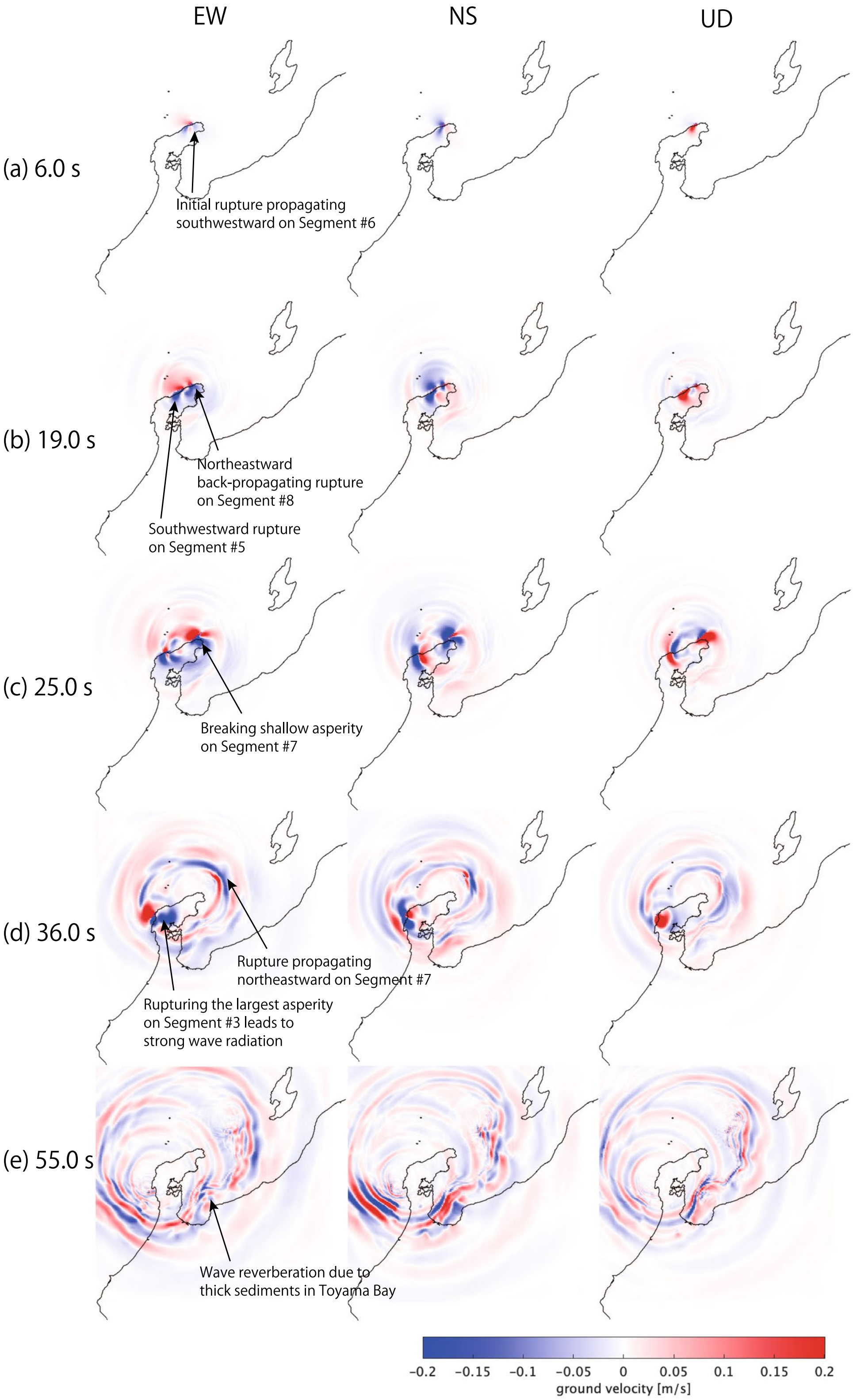

Fig. 3 Snapshots of three-component ground velocities on the Earth's surface for the best-fit source model, taken at $T_0 +$ indicated times. The ground motions reflect the combined effects of complex rupture evolution and 3D velocity structure, including influences from low-velocity sediments. Time zero corresponds to the origin time assumed in this study (07:10:09.5 UTC)

Fig. 3. During the first 10 s of the mainshock, the ground motion is mainly generated by thrust faulting with southwestward rupture propagation (Fig. 3a). Between $T_0 + 10$ and $T_0 + 20$ s, the ground motion reflects the presence of multiple rupture fronts, producing a complex spatiotemporal pattern near the source region (Fig. 3b). In particular, around $T_0 = 19$ s, the ground motion signature of the backward rupture on Segment #8 can be seen (Fig. 3b). Between $T_0 + 20$ and $T_0 + 30$ s, nearly simultaneous ruptures of the northeastern (Segment #7) and southwestern (Segment #4) large slip patches generated two distinct wavefields (Fig. 3c). The most intense wave radiation around T0 + 36 s can be identified as a result of breaking the largest asperity offshore Monzen (Fig. 3d), which leads to the emergence of the second large phase at around T0 + 40 s at some stations (e.g., 7018 (Fig. 2b) and KH03 (Fig. S9)). Seismic waves encountered thick, low-velocity sediments in Toyama Bay, resulting in wave reverberations and prolonged velocity waveforms (Fig. 3e), as observed at stations in Toyama and Niigata (Fig. S9).

4 Discussion

4.1 Best-fitting model's validity and limitation

The best-fitting model accurately reproduces the observed waveforms, especially at near-fault stations. Compared to waveforms calculated using the USGS finite fault model and a simple source model, the best-fitting model better matches the onset, amplitude, and polarity of the main phases in the observed records. Furthermore, it successfully explains the unfiltered displacement waveforms recorded at 1-Hz GNSS stations (Fig. S11), which are not included in the waveform fitting process, reinforcing the validity of this source model. Notably, the assumed final slip distribution from the geodetically constrained slip model (Fukushima et al. 2024) does not require modification and simple, quasi-circular rupture propagation on individual fault segments is sufficient to reproduce the comprehensive set of strong-motion and high-rate GNSS waveforms.

While the overall fit to the waveforms is adequate and the inferred southwestward rupture propagation on the southern fault segments (#1 to #5) is well-constrained by the data, notable waveform misfits are observed in the swarm region (e.g., Stations K002 and KH03). However, synthetic waveforms fit the observed data well at longer periods ($\geq$6 s) (Fig. S12), indicating that the best-fitting model effectively resolves the rupture process at scales of $\geq$9 km, assuming $V_r = 1.5$ km/s. Hence, the discrepancy at shorter periods may result from a more complex rupture process involving intermittent arrest and restart, rather than the simple quasi-circular rupture assumed in this study, and/or the activation of two sub-parallel dipping faults during the mainshock, as inferred from the relocation of early aftershocks (Yoshida et al. 2024). Although our assumption that a single fault plane slipped twice might not be accurate, a recent study utilizing tsunami waveform inversion and multiple CMT solutions (Kutschera et al. 2024) also supports the occurrence of two distinct slip episodes originating from the same location in the swarm region within the initial 25 s of the mainshock, consistent with our interpretation of the multiple slip episodes on the same fault plane.

In addition, the slip distribution and rupture episode on the offshore portion of Segment #7 are likely oversimplified due to uncertainties in fault geometry and slip distribution, which are not well-constrained by inland geodetic data. Future studies could incorporate tsunami waveform inversion (Fujii and Satake 2024; Kutschera et al. 2024) to better constrain the fault geometry and slip characteristics in the offshore segment.

4.2 Relationship between the rupture processes and the swarm activity in the Noto region

In the best-fitting model, fault segments near the mainshock hypocenter is characterized by complex rupture evolution with multiple rupture fronts activated at a given instant in time, consistent with previously reported earthquake swarm zones (Nishimura et al. 2023; Yoshida et al. 2023). Our best-fitting model shows that the mainshock hypocenter and the initiation points of the subsequent ruptures are located at the edges of these swarm zones (Fig. 4). While the relevance of the $M_{\mathrm{jma}}7.6$ hypocenter and these rupture initiation points remains unclear, the $M_{\mathrm{jma}}7.6$ hypocenter is also situated at the edge of the earthquake swarm (Fig. S13). The spatial correlation between rupture initiation points and the edges of earthquake swarms suggests that ruptures on different segments originated in areas of increased shear stress at the periphery of preceding swarm activity. The ruptures propagating through the swarm region on Segments #6 and #8 may have been intermittent, likely due to the heterogeneous distribution of prestress, strength (Aki 1984), frictional properties (Ito and Kaneko 2023), or a combination of these factors. Such heterogeneities would have contributed to the delayed onset of the northeastward rupture on Segment #7 and the re-rupture of the same fault segments (#6 and #8) within the earthquake swarm region (Fig. 4).

4.3 On multiple slip episodes on a fault segment

The fault segment (#6) near the mainshock hypocenter ruptured twice, with the first and second ruptures contributing 30% and 70% of the segment's total moment release, respectively (Fig. 4a, b). Re-rupturing of the same fault segment during a large earthquake is a rare

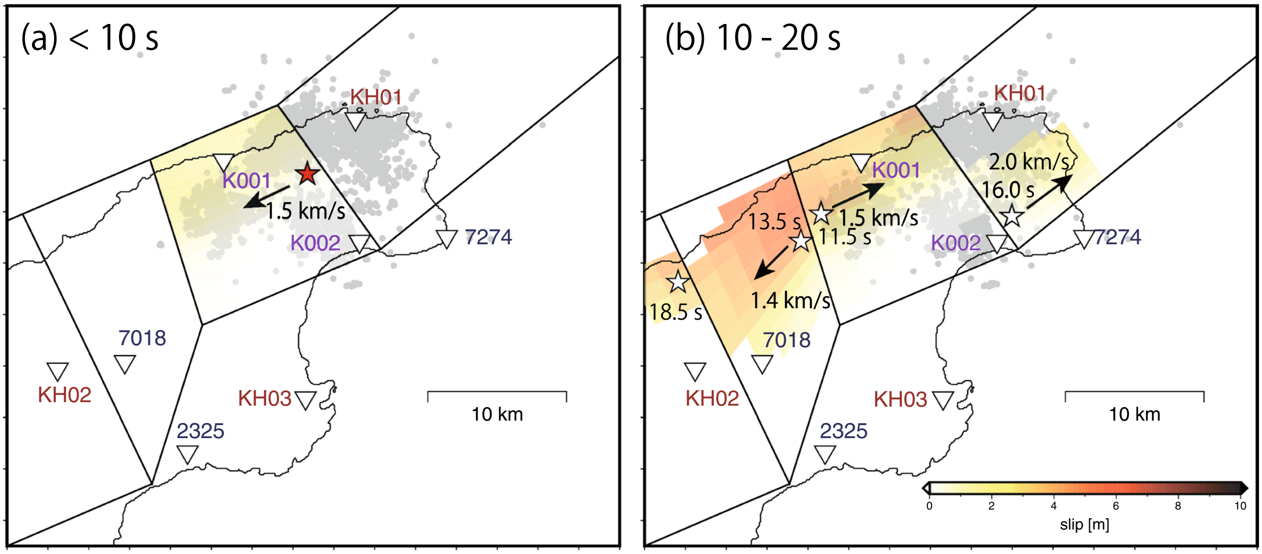

Fig. 4 Comparison of slip and rupture evolution near the epicenter in the best-fitting model with the locations of pre-mainshock earthquake swarms, based on the relocated catalog (Yoshida et al. 2023). Red stars indicate the epicenter, while white stars denote the rupture initiation points for individual fault segments. Arrows and associated labels illustrate the along-strike direction and rupture propagation speed for each segment. The rupture initiation locations (red and white stars) are situated near the edges or gaps of the swarm regions. Time zero corresponds to the origin time assumed in this study (07:10:09.5 UTC)

occurrence, as fault slip typically reduces the shear stress. However, a similar phenomenon was observed on the Kekerengu fault during the 2016 Mw 7.8 Kaikoura earthquake in New Zealand, where the second rupture was larger than the first, as constrained by near-fault strong-motion data (Holden et al. 2017). Unlike the Noto earthquake, the Kekerengu fault did not experience preceding swarm activity, suggesting different underlying mechanisms for the re-rupturing in these events. Numerical models of foreshock generation with fault frictional heterogeneities (Ito and Kaneko 2023) indicate that foreshock sizes can increase over time, on average, due to afterslip from preceding numerous foreshocks, which promotes coseismic rupture propagation through these slowly slipping barriers, eventually culminating in a larger rupture (i.e., the mainshock). For the Noto earthquake, the mainshock was preceded by numerous foreshocks (Peng et al. 2024), suggesting that fault creep or afterslip induced by these foreshocks and swarm activities may have facilitated the re-rupturing of the same fault segment during the mainshock. The presence of such slip heterogeneities is evidenced by complex, multi-phase waveforms observed at epicentral stations (e.g., Stations K001 and K002), which are difficult to reconcile with our simplified rupture model (Fig. S14b).

4.4 Comparison with finite-fault models in previous studies

Our preferred model shares similarities and differences with previously published source models of the Noto mainshock (Okuwaki et al. 2024; Ma et al. 2024; Xu et al. 2024). The moment rate function in Okuwaki et al. (2024) features three peaks: two associated with minor and major rupture events in the southern fault area, followed by a third, highest peak at approximately $T_0 + 30$ s, resulting from combined slips in the southern and northern fault sections. Similarly, Xu et al. (2024) and Ma et al. (2024) describe moment rate functions with two peaks: the first corresponding to an initial rupture near the hypocenter, and the second to a distant fault patch, both peaking around $T_0 + 30$ s. A key difference is that Xu et al. (2024) incorporates a large slip patch in the northern fault, while Ma et al. (2024) omits it entirely.

In contrast, the moment rate function in our best-fitting model shows four distinct peaks at $T_0 + 7$, 25, 34, and 42 s (Fig. 2f). The primary difference from previous studies lies in the timing of the highest peak: in our model, it occurs at $T_0 + 25$ s, compared to $T_0 + 30$ to $T_0 + 35$ s in other models. This discrepancy arises from an earlier rupture of a large slip patch in the northern fault in our model, which contributes to the earlier peak. In contrast, Ma et al. (2024) excludes this slip patch, and

Xu et al. (2024) positions it farther northeast of the hypocenter, delaying the peak. We note that the shallow asperity on Segment #7, which contributes to the $T_0 + 25$ s peak in our model, is well-resolved by on-land geodetic data (Fig. S2), and the timing of the rupture is well-constrained by waveform fits at nearby stations, such as Station KH01 (Fig. S9).

The first 20 s of the mainshock rupture differ significantly among source models. While all source models, including ours, depict a quiet start in the first 10 s (Fig. 2f), our model estimates a faster rupture speed in the epicentral region (1.5 km/s) than the 0.5 km/s and 0.8 km/s inferred by Ma et al. (2024) and Xu et al. (2024), respectively. Differences in assumed hypocenters (Fig. S13) are too small to explain these discrepancies, but Xu et al. (2024)'s finite fault model assumes an origin time 1.2 s earlier than ours, partly contributing to the difference. To test slow initial rupture propagation, we vary rupture speed ($V_{\mathrm{r}6}$) from 0.3 to 2.1 km/s (Fig. S8e), identifying a local misfit minimum at $V_{\mathrm{r}6} = 0.4$ km/s (Fig. S8e) with corresponding waveform fits in Fig. S14a. While a slower rupture speed or more complex rupture behavior involving intermittent arrest and restart cannot be ruled out due to limited resolution from the configuration of strong-motion stations in this region, this slow rupture model cannot explain early phases in the first 10 s in the nearby strong-motion stations (e.g., K001) (Fig. S14a, b). We note that our inference of the ruptures being initiated at the edges of the preceding swarm zone is not affected by non-uniqueness in the initial rupture speed (Fig. S14c, d).

Similar to Xu et al. (2024), our best-fitting source model also exhibits back-propagating rupture toward the mainshock hypocenter. However, the locations of large slip patches differ significantly. In our source model, slip on the relevant fault segments is more smoothly distributed, with a maximum slip of approximately 6 m, and the 14-m slip patch responsible for the back-propagating rupture in Xu et al. (2024) is absent. In addition, the timing of the backward rupture initiation in our model aligns with the arrival of the first rupture propagating southwestward on Segment #6, contradicting the previous inference of dual-initiation ruptures (Xu et al. 2024). We attribute the back-propagating rupture to the abrupt change in the local fault geometry at the boundary between Segments #5 and #6, consistent with numerical studies suggesting that non-planar fault geometry can induce backward-propagating ruptures (Madariaga et al. 2006; Ding et al. 2024).

To examine discrepancies between published source models and our best-fitting model, we perform additional wavefield simulations using the source models of Ma et al. (2024) and Xu et al. (2024), assuming the same velocity and attenuation structure (Section S1). The corresponding synthetic velocity waveforms fit well at stations used in their finite-fault inversions but not at others (Fig. 5 and Fig. S15–S18; Section S1). The total misfits for all stations are $\chi = 2.060$ for Ma et al. (2024) (Fig. S15) and $\chi = 2.014$ for Xu et al. (2024) (Fig. S17), both exceeding $\chi = 1.464$ for our best-fitting model (Fig. S9). Large waveform misfits at near-fault stations (Fig. 5) suggest velocity structure differences are not the main cause, but rather variations in fault geometries, station selection, and source modeling assumptions, where each sub-fault is parameterized by local rise time, slip, and rupture time (Ji et al. 2003). While our quasi-circular rupture propagation and rise time-slip scaling are simplifications, fewer free parameters may have mitigated trade-offs and non-uniqueness (Ozgun Konca et al. 2013; Mai et al. 2016). These results also highlight the importance of near-fault strong-motion data for accurate source modeling.

As stated above, one of the primary sources of discrepancies among various source models likely stems from differences in the assumed or inferred fault geometries (Fig. 5). Previous studies (Ma et al. 2024; Xu et al. 2024) positioned fault segments farther offshore from the Noto Peninsula, requiring larger slip beneath the peninsula to match on-land strong-motion waveforms (Fig. 5). In contrast, the fault geometry and final slip distribution used in this study, adopted from Fukushima et al. (2024), may be better constrained than those of other models (Okuwaki et al. 2024; Ma et al. 2024; Xu et al. 2024), as it incorporates both near- and far-field geodetic data (Fig. S2). While the fault geometry for the northeastern offshore segment (Segment #7) remains less well-constrained, the other fault segments, primarily beneath the Noto Peninsula, achieve a resolution of a few kilometers, particularly within the top 10 km (Fig. S10–S12 of Fukushima et al. (2024)), aligning with the spatial scale relevant for 4-s velocity waveforms.

5 Conclusions

We developed a kinematic rupture model of the 2024 Noto Peninsula earthquake by integrating seismic wavefield simulations, a comprehensive set of near-field strong-motion and high-rate GNSS data, and a static slip model constrained by geodetic data. Our best-fitting model reveals multiple large slip patches and distinct rupture episodes, with propagation speeds ranging from 1.4 to 2.1 km/s—slower than typical intraplate earthquakes—indicating a complex rupture process during the mainshock. The fault segment near the epicentral region exhibits multiple slip episodes and intricate rupture evolution. In particular, our result suggests that the mainshock hypocenter and the initiation points of subsequent ruptures are located in

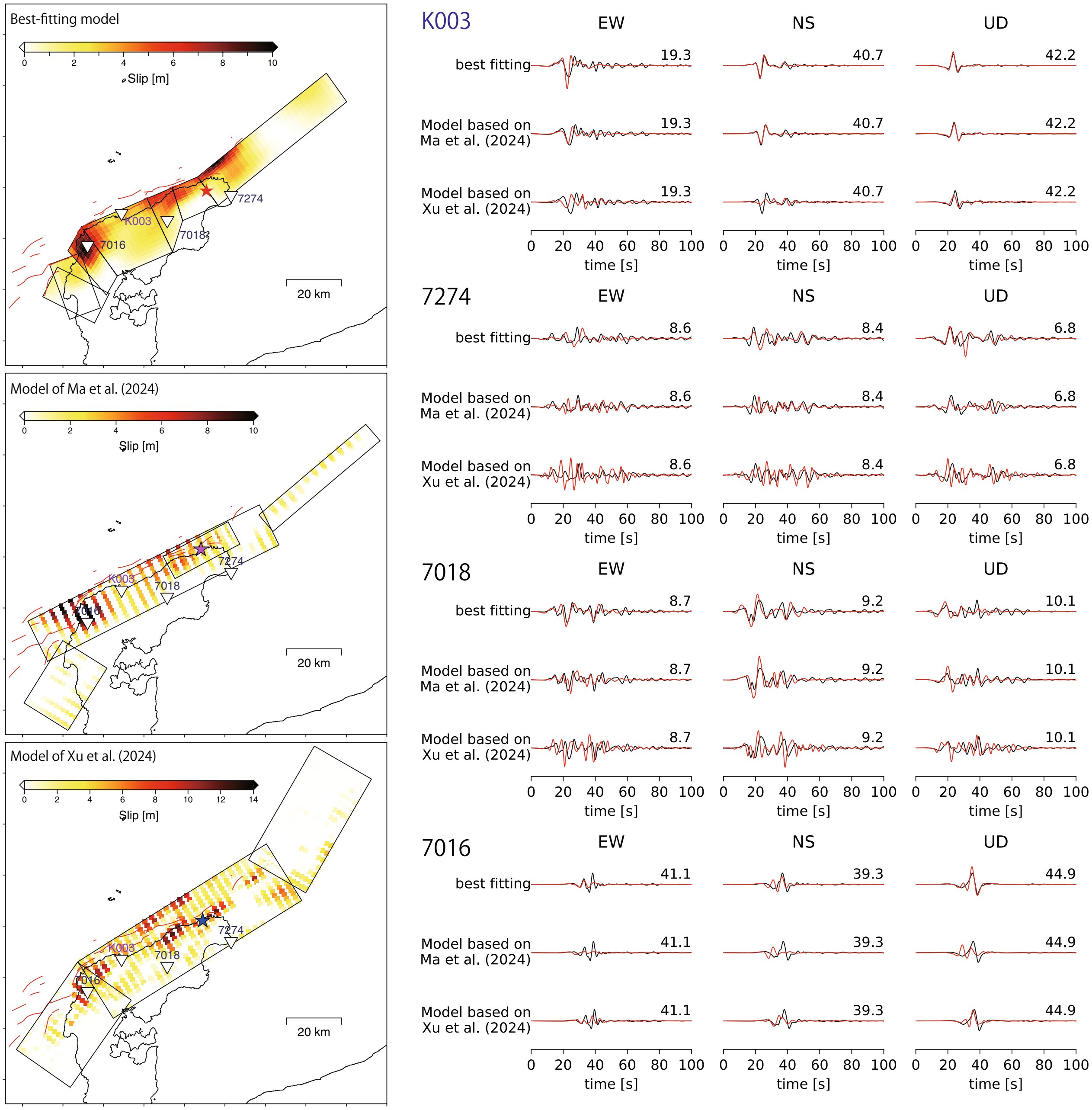

Fig. 5 Comparison of waveform fits at selected stations among the best-fitting model, the Ma et al. (2024) model, and the Xu et al. (2024) model. Stars indicate the epicenters in the respective models. Inverted triangles indicate strong-motion stations. Station K003 (in blue) was used in all three studies, while Stations 7274, 7018, and 7016 (in black) were not used in the finite fault inversions by Ma et al. (2024) and Xu et al. (2024). All waveforms are filtered to a period range of 4–20 s and normalized to the maximum amplitude of the observed waveform at each station (normalization factor in cm/s shown on the right of each waveform). Time zero corresponds to the origin time assumed in each respective source model (Table S1). Stations used in the respective finite-fault inversions show good fits, while those not used exhibit poorer fits. Waveform fits at other stations are shown in Fig. S15–S18

areas of increased shear stresses in the periphery of the preceding swarm activity. In addition, the inferred backward-propagating rupture in the epicentral region may have been triggered by an abrupt change in local fault geometry. Further investigations, including offshore fault imaging and seafloor offset surveys, are crucial to refining our understanding of this complex rupture process.

Supplementary Information

The online version contains supplementary material available at https://doi.org/10.1186/s40623-025-02213-w.

Supplementary Material 1.

Acknowledgements
We thank Editor Aitaro Kato and two anonymous reviewers for their valuable comments, which helped improve the manuscript. We also appreciate Jesse Kearse and Yoshito Nozuka for their insightful discussions. In addition, we thank Keisuke Yoshida for providing the relocated hypocenters of seismicity in the Noto region.

Author contributions
Y.K. and R.E. designed the study. R.E. and Y.K. analyzed the strong-motion data, constructed the mesh, performed numerical simulations, interpreted the results, and drafted the manuscript. C.-H.T. and Y.F. provided the static slip model and contributed to interpretations. H.G. processed KiK-net and K-NET strong-motion data, while S.M. processed high-rate GNSS data. All authors contributed to analyzing and discussing the results and to the preparation of the manuscript.

Funding
Research was supported by JSPS KAKENHI (21H05206), and ERI JURP 2024-S-B103 and 2024-S-B301 in Earthquake Research Institute, the University of Tokyo.

Availability of data and materials
The ground motion data (K-NET and KiK-net) are available from National Research Institute for Earth Science and Disaster Resilience (https://www.kyoshin.bosai.go.jp/kyoshin/), and Japan Meteorological Agency (https://www.data.jma.go.jp/eqev/data/kyoshin/jishin/2401011612_noto/index.html). The high-rate (1 Hz) GNSS data are available from Japan GPS Data Service (https://www.gpsdata.co.jp) and were processed using GipsyX (Bertiger et al. 2020). Wave propagation software SPECFEM3D is available at https://github.com/SPECFEM/specfem3d. Numerical data used to produce all the figures are available at https://zenodo.org/records/14917516.

Declarations

Competing interests
The authors declare no competing interests.

Author details
[1]Graduate School of Science, Kyoto University, Kyoto, Japan. [2]International Research Institute of Disaster Science, Tohoku University, Sendai, Japan. [3]Disaster Prevention Research Institute, Kyoto University, Kyoto, Japan.

Received: 2 December 2024 Accepted: 11 May 2025

References

Aki K (1984) Asperities, barriers, characteristic earthquakes and strong motion prediction. J Geophys Res Solid Earth 89(B7):5867–5872. https://doi.org/10.1029/JB089iB07p05867

Amezawa Y, Hiramatsu Y, Miyakawa A et al (2023) Long-living earthquake swarm and intermittent seismicity in the northeastern tip of the Noto Peninsula, Japan. Geophys Res Lett 50(8):e2022GL102670. https://doi.org/10.1029/2022GL102670

Asano K, Iwata T (2011) Source-rupture process of the 2007 Noto Hanto, Japan, earthquake estimated by the joint inversion of strong motion and GPS data. Bull Seismol Soc Am 101(5):2467–2480. https://doi.org/10.1785/0120100254

Bertiger W, Bar-Sever Y, Dorsey A et al (2020) GipsyX/RTGx, a new tool set for space geodetic operations and research. Adv Space Res 66(3):469–489. https://doi.org/10.1016/j.asr.2020.04.015

Ding X, Xu S, Fukuyama E et al (2024) Back-propagating rupture: Nature, excitation, and implications. J Geophys Res Solid Earth 129(10):e2024JB029629. https://doi.org/10.1029/2024JB029629

Fire and Disaster Management Agency (2024) Damage caused by the Noto Peninsula earthquake of 2024 and the response of fire-fighting agencies. (Report No. 111). https://www.fdma.go.jp/disaster/info/2024/

Fujii Y, Satake K (2024) Slip distribution of the 2024 Noto Peninsula earthquake (M_{JMA} 7.6) estimated from tsunami waveforms and GNSS data. Earth Planets Space 76(1):44. https://doi.org/10.1186/s40623-024-01991-z

Fukushima Y, Ishimura D, Takahashi N et al (2024) Landscape changes caused by the 2024 Noto Peninsula earthquake in Japan. Science Advances 10(49):eadp9193. https://doi.org/10.1126/sciadv.adp9193

Graves RW, Pitarka A (2010) Broadband ground-motion simulation using a hybrid approach. Bull Seismol Soc Am 100(5A):2095–2123. https://doi.org/10.1785/0120100057

Hiramatsu Y, Moriya K, Kamiya T et al (2008) Fault model of the 2007 Noto Hanto earthquake estimated from coseismic deformation obtained by the distribution of littoral organisms and GPS: Implication for neotectonics in the northwestern Noto Peninsula. Earth Planets Space 60:903–913. https://doi.org/10.1186/BF03352846

Hjörleifsdóttir V, Kanamori H, Tromp J (2009) Modeling 3-D wave propagation and finite slip for the 1998 Balleny Islands earthquake. J Geophys Res Solid Earth. https://doi.org/10.1029/2008JB005975

Holden C, Kaneko Y, D'Anastasio E et al (2017) The 2016 Kaikōura earthquake revealed by kinematic source inversion and seismic wavefield simulations: slow rupture propagation on a geometrically complex crustal fault network. Geophys Res Lett 44(22):11–320. https://doi.org/10.1002/2017GL075301

Inoue T, Okamura Y (2010) Explanatory notes of 1: 200,000 marine geological map around the northern part of Noto Peninsula, seamless geoinformation of coastal zone "northern coastal zone of Noto Peninsula" (DVD), digital geoscience map S-1

Ito R, Kaneko Y (2023) Physical mechanism for a temporal decrease of the Gutenberg-Richter b-value prior to a large earthquake. J Geophys Res Solid Earth 128(12):e2023JB027413. https://doi.org/10.1029/2023JB027413

Ji C, Helmberger DV, Wald DJ et al (2003) Slip history and dynamic implications of the 1999 Chi-Chi, Taiwan, earthquake. J Geophys Res Solid Earth. https://doi.org/10.1029/2002JB001764

Kaneko Y, Goto H (2022) The origin of large, long-period near-fault ground velocities during surface-breaking strike-slip earthquakes. Geophys Res Lett 49(10):e2022GL098029. https://doi.org/10.1029/2022GL098029

Kato A, Obara K (2014) Step-like migration of early aftershocks following the 2007 Mw 6.7 Noto-Hanto earthquake, Japan. Geophys Res Lett 41(11):3864–3869. https://doi.org/10.1002/2014GL060427

Kato A, Sakai S, Iidaka T et al (2008) Three-dimensional velocity structure in the source region of the Noto Hanto Earthquake in 2007 imaged by a dense seismic observation. Earth Planets Space 60:105–110. https://doi.org/10.1186/BF03352769

Kato A, Sakai S, Iidaka T et al (2011) Anomalous depth dependency of the stress field in the 2007 Noto Hanto, Japan, earthquake: Potential involvement of a deep fluid reservoir. Geophys Res Lett. https://doi.org/10.1029/2010GL046413

Koketsu K, Miyake H, Suzuki H (2012) Japan integrated velocity structure model version 1. In: Proceedings of the 15th world conference on earthquake engineering, Lisbon. p. 4

Kutschera F, Jia Z, Oryan B et al (2024) The Multi-Segment Complexity of the 2024 Mw 7.5 Noto Peninsula Earthquake Governs Tsunami Generation. Geophys Res Lett 51(21):e2024GL109790. https://doi.org/10.1029/2024GL109790

Ma Z, Zeng H, Luo H et al (2024) Slow rupture in a fluid-rich fault zone initiated the 2024 Mw 7.5 Noto earthquake. Science 385(6711):866–871. https://doi.org/10.1126/science.ado5143

Madariaga R, Ampuero J, Adda-Bedia M (2006) Seismic radiation from simple models of earthquakes. Geophys Monogr Am Geophys Union 170:223

Mai PM, Schorlemmer D, Page M et al (2016) The earthquake-source inversion validation (SIV) project. Seismol Res Lett 87(3):690–708. https://doi.org/10.1785/0220150231

Masuda H, Sugawara D, Cheng AC et al (2024) Modeling the 2024 Noto Peninsula earthquake tsunami: implications for tsunami sources in the eastern margin of the Japan Sea. Geosci Lett 11(1):29. https://doi.org/10.1186/s40562-024-00344-8

Nishimura T, Hiramatsu Y, Ohta Y (2023) Episodic transient deformation revealed by the analysis of multiple GNSS networks in the Noto Peninsula, central Japan. Sci Rep 13(1):8381. https://doi.org/10.1038/s41598-023-35459-z

Okamura Y, Watanabe M, Morijiri R et al (1995) Rifting and basin inversion in the eastern margin of the Japan Sea. Island Arc 4(3):166–181. https://doi.org/10.1111/j.1440-1738.1995.tb00141.x

Okuwaki R, Yagi Y, Murakami A et al (2024) A multiplex rupture sequence under complex fault network due to preceding earthquake swarms during the 2024 Mw 7.5 Noto Peninsula, Japan, earthquake. Geophys Res Lett 51(11):e2024GL109224. https://doi.org/10.1029/2024GL109224

Ozgun Konca A, Kaneko Y, Lapusta N et al (2013) Kinematic inversion of physically plausible earthquake source models obtained from dynamic rupture simulations. Bull Seismol Soc Am 103(5):2621–2644

Peng Z, Lei X, Wang QY et al (2024) The Evolution Process between the Earthquake Swarm Beneath the Noto Peninsula, Central Japan and the 2024 M 7.6 Noto Hanto Earthquake Sequence. Earthquake Res Adv. https://doi.org/10.1016/j.eqrea.2024.100332

Peter D, Komatitsch D, Luo Y et al (2011) Forward and adjoint simulations of seismic wave propagation on fully unstructured hexahedral meshes. Geophys J Int 186(2):721–739. https://doi.org/10.1111/j.1365-246X.2011.05044.x

Sato H (1994) The relationship between late Cenozoic tectonic events and stress field and basin development in northeast Japan. J Geophys Res Solid Earth 99(B11):22261–22274. https://doi.org/10.1029/94JB00854

Xu L, Ji C, Meng L et al (2024) Dual-initiation ruptures in the 2024 Noto earthquake encircling a fault asperity at a swarm edge. Science 385(6711):871–876. https://doi.org/10.1126/science.adp0493

Yoshida K, Uno M, Matsuzawa T et al (2023) Upward earthquake swarm migration in the northeastern Noto Peninsula, Japan, initiated from a deep ring-shaped cluster: Possibility of fluid leakage from a hidden magma system. J Geophys Res Solid Earth 128(6):e2022JB026047. https://doi.org/10.1029/2022JB026047

Yoshida K, Takagi R, Fukushima Y et al (2024) Role of a hidden fault in the early process of the 2024 Mw7.5 Noto Peninsula earthquake. Geophys Res Lett 51(16):e2024GL110993. https://doi.org/10.1029/2024GL110993

Publisher's Note

Supporting Information for "Multi-Fault Segment Complexity and Multi-Rupture Episodes during the 2024 Mw 7.5 Noto Peninsula Earthquake"

Rintaro Enomoto, Graduate School of Science, Kyoto University, Japan, enomoto.rintaro.42n@st.kyoto-u.ac.jp

Yoshihiro Kaneko, Graduate School of Science, Kyoto University, Japan, kaneko.yoshihiro.4e@kyoto-u.ac.jp

Chi-Hsien Tang, International Research Institute of Disaster Science, Tohoku University, Japan, tang.chi-hsien.b8@tohoku.ac.jp

Yo Fukushima, International Research Institute of Disaster Science, Tohoku University, Japan, fukushima@irides.tohoku.ac.jp

Hiroyuki Goto, Disaster Prevention Research Institute, Kyoto University, Japan, goto.hiroyuki.3z@kyoto-u.ac.jp

Shin'ichi Miyazaki, Graduate School of Science, Kyoto University, Japan, miyazaki.shinichi.2m@kyoto-u.ac.jp

Preprint submitted to *Earth, Planets and Space* on April 21, 2025

Contents of this file

S1 Waveform Calculation of Previous studies

Wavefield simulations based on the source models of Ma et al (2024) and Xu et al (2024) are set up as follows. We extract the strike, dip, rake, slip, and area of each sub-fault from the respective finite-fault models and convert them to moment tensors, assuming the same shear modulus distribution as in our study. The centroid time of each point source is calculated as:

$$T_{\mathrm{CMT}} = T_{\mathrm{rup}} + \frac{T_{\mathrm{rise}}}{2}$$

where T_{rup} is the rupture start time of each sub-fault and T_{rise} is the local rise time. Since Xu et al (2024) used an asymmetric cosine function to approximate the derivative of the rise time (Ji et al 2003), we assume that T_{rise} is the sum of the starting-phase and end-phase times in the asymmetric cosine function (Ji et al 2003). For the Ma et al (2024) source file downloaded from https://zenodo.org/records/11314960, a +11.5 s time shift to T_{rup} was required for their fault segments #2–4 to match the moment rate function shown in Ma et al (2024). Applying this adjustment aligns the main phases between the synthetic and observed waveforms at the stations used in the finite-fault inversion by Ma et al (2024).

The source models of Ma et al (2024) and Xu et al (2024) yield larger waveform misfits than our best-fitting model, with misfit values of $\chi = 1.464$ for the besting fitting model (Figure S9), $\chi = 2.060$ for Ma et al (2024) (Figure S15) and $\chi = 2.014$ for Xu et al (2024) (Figure S17), respectively However, when considering only the stations used in their respective inversions, the misfits reduce to $\chi = 1.573$ for the Ma et al (2024) model (Figure S15) and $\chi = 1.475$ for the Xu et al (2024) model (Figure S17), which are comparable to the best-fitting model. Longer-period (10 – 50 s) waveforms exhibit better agreement with observed data (Figures S16 and S18), consistent with the best-fitting model. These results highlight the importance of incorporating numerous near-fault strong-motion data to develop an accurate source model.

Source model	Segment	Dip angle [°]	Rupture-start point (Lon [°], Lat [°], depth [km])	Vr [km/s]	Rupture timing [s]	χ	M_w
USGS	-	-	-	-	7:10:09.0	3.299	
Simple rupture with $V_\mathrm{r} = 2.0$ km/s	#1 - 7	-	137.2451, 37.4911, 8.7	2.0	7:10:09.5	2.363	
Best-fitting model	#1, #2	#1: 45, #2: 45	136.7693, 37.1946, 10.6	1.7	7:10:09.5 +36.0	1.464	#1: 6.14, #2: 6.65
	#3	45	136.7917, 37.3068, 7.3	2.0	7:10:09.5 +32.8		6.99
	#4	43	137.0274, 37.4209, 4.7	2.1	7:10:09.5 +18.5		7.15
	#5	54 (average)	137.1276, 37.4475, 8.7	1.4	7:10:09.5 +13.5		6.92
	#6	58	137.2451, 37.4911, 8.7	1.5	7:10:09.5		6.44
	#7	58	137.2998, 37.4636, 16.7	2.0	7:10:09.5 +16.0		7.21
	#8	58	137.1443, 37.4651, 7.3	1.5	7:10:09.5 +11.5		6.68
Ma et al (2024)	-	-	-	-	7:10:09.0	2.060	
Xu et al (2024)	-	-	-	-	7:10:08.33	2.014	

Table S1. Table listing rupture speed (V_r) and rupture start time (T) for each source model, along with the corresponding waveform misfit (χ). In the simple rupture model with $V_\mathrm{r} = 2.0$ km/s and the best-fitting model, the rupture starting point of fault segment #6 corresponds to the mainshock hypocenter.

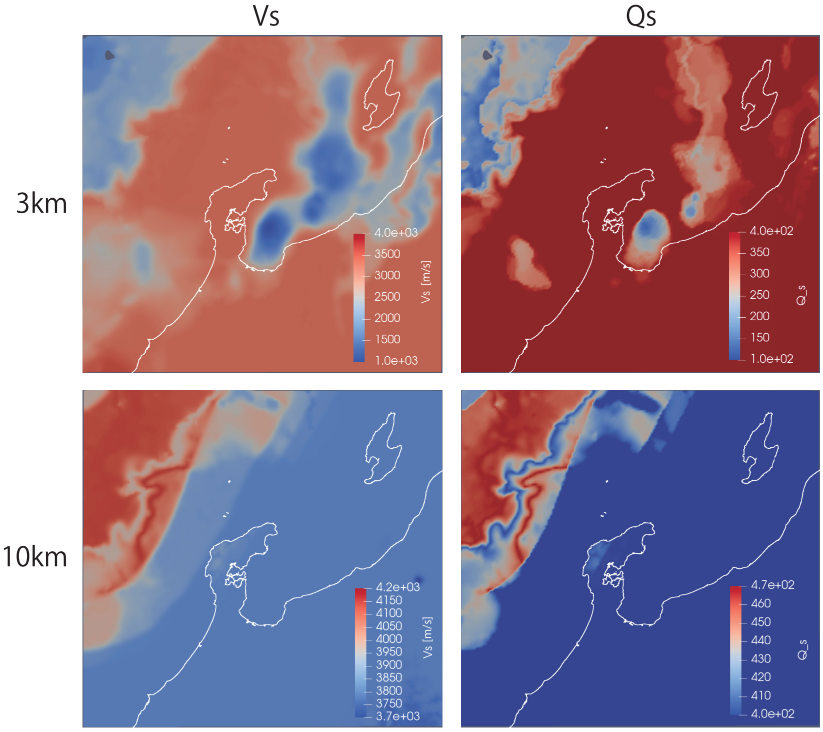

Figure S1. Maps of S-wave velocity V_s and shear quality factor Q_s at depths of 3 km and 10 km. A prominent low-V_s region extends down several kilometers in Toyama Bay, which also corresponds to a low-Q_s area in the same region.

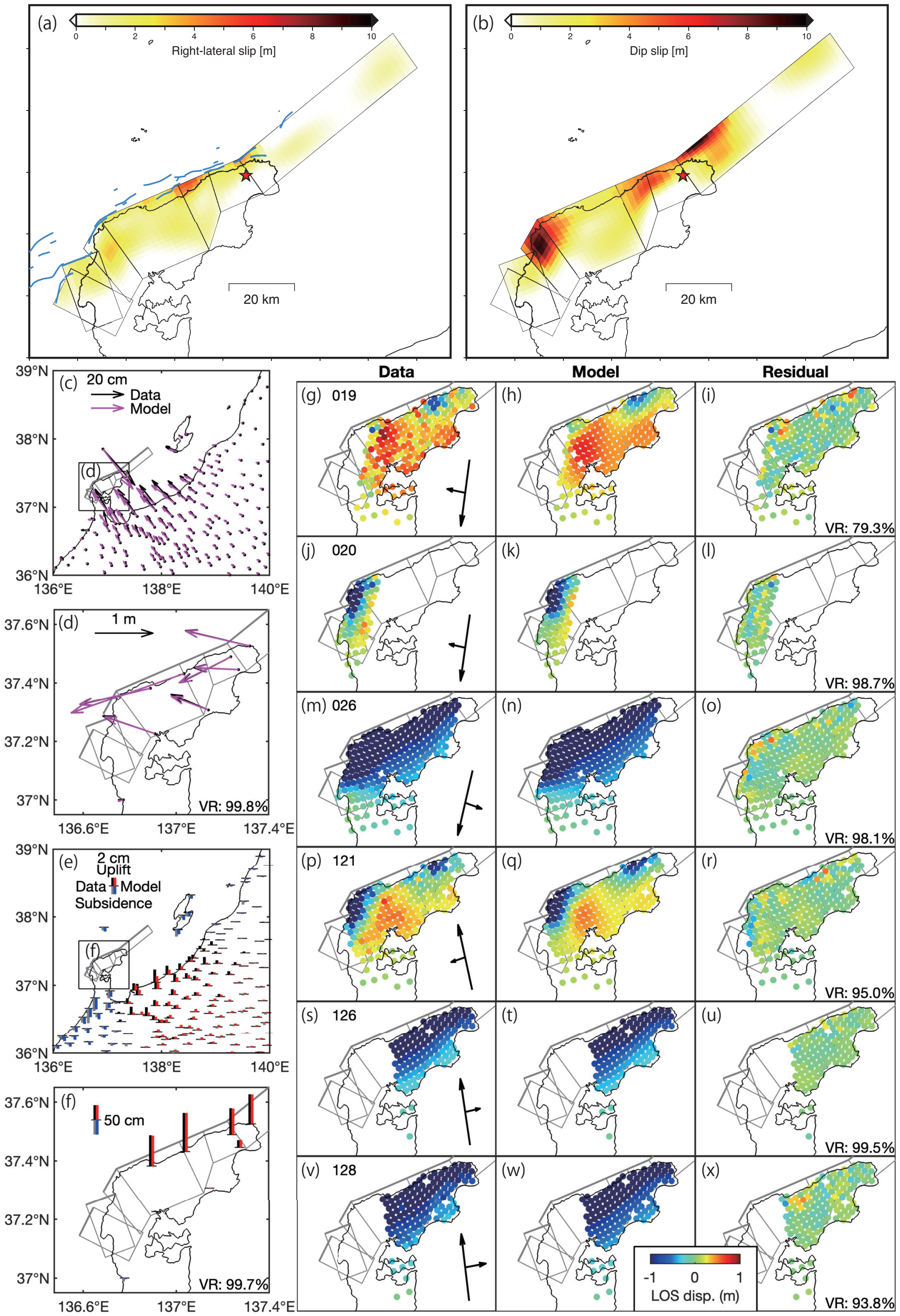

Figure S2. Slip distribution and fault geometry derived from the inversion of geodetic data from Fukushima et al (2024), showing (a) the right-lateral strike-slip component, (b) the dip-slip component, and (c–x) corresponding surface displacements compared to geodetic observations. Panels (c–f) illustrate the fit between modeled and observed horizontal and vertical GNSS data, while (g–x) present the comparison between SAR data and modeled coseismic displacements. Arrows indicate satellite flight and line-of-sight (LOS) directions, and variance reduction (VR) values are provided. Modified from Figures S7–S9 of Fukushima et al (2024).

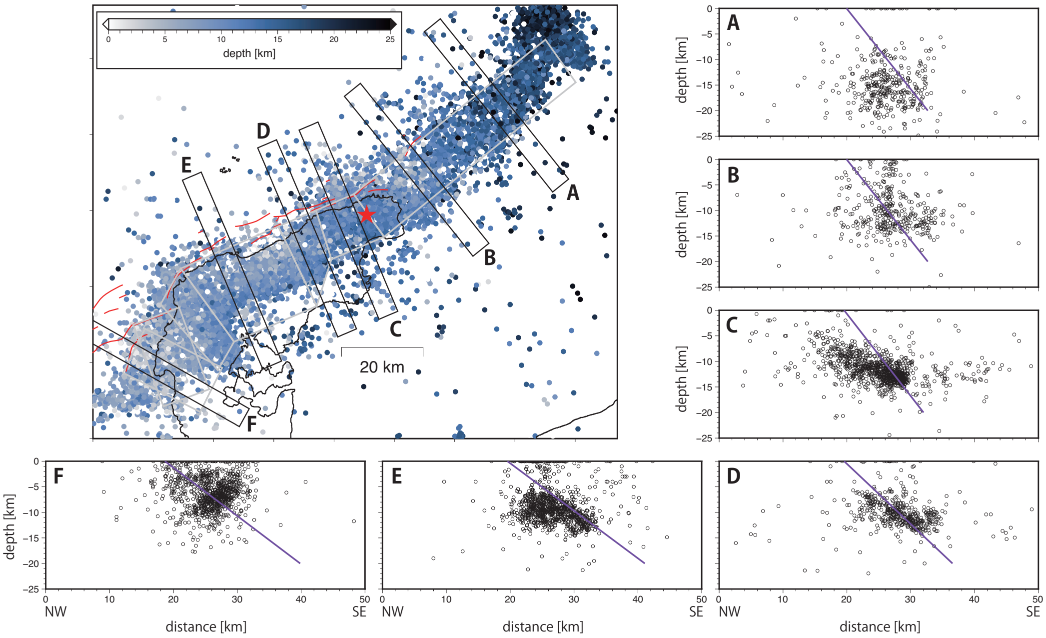

Figure S3. Epicenters of the Mw 7.5 Noto mainshock and subsequent aftershocks (recorded up to January 31, 2024, 23:59 JST), sourced from the Japan Meteorological Agency (JMA) catalog. The star marks the mainshock, while circles represent aftershocks, with color indicating the depth of their hypocenters. Although the JMA reported two possible origin times for the mainshock (16:10:09.5 JST and 16:10:22.5 JST), we use 16:10:09.5 JST as the origin time in this study. In each cross-section, the fault plane location assumed in this study is shown by the purple line.

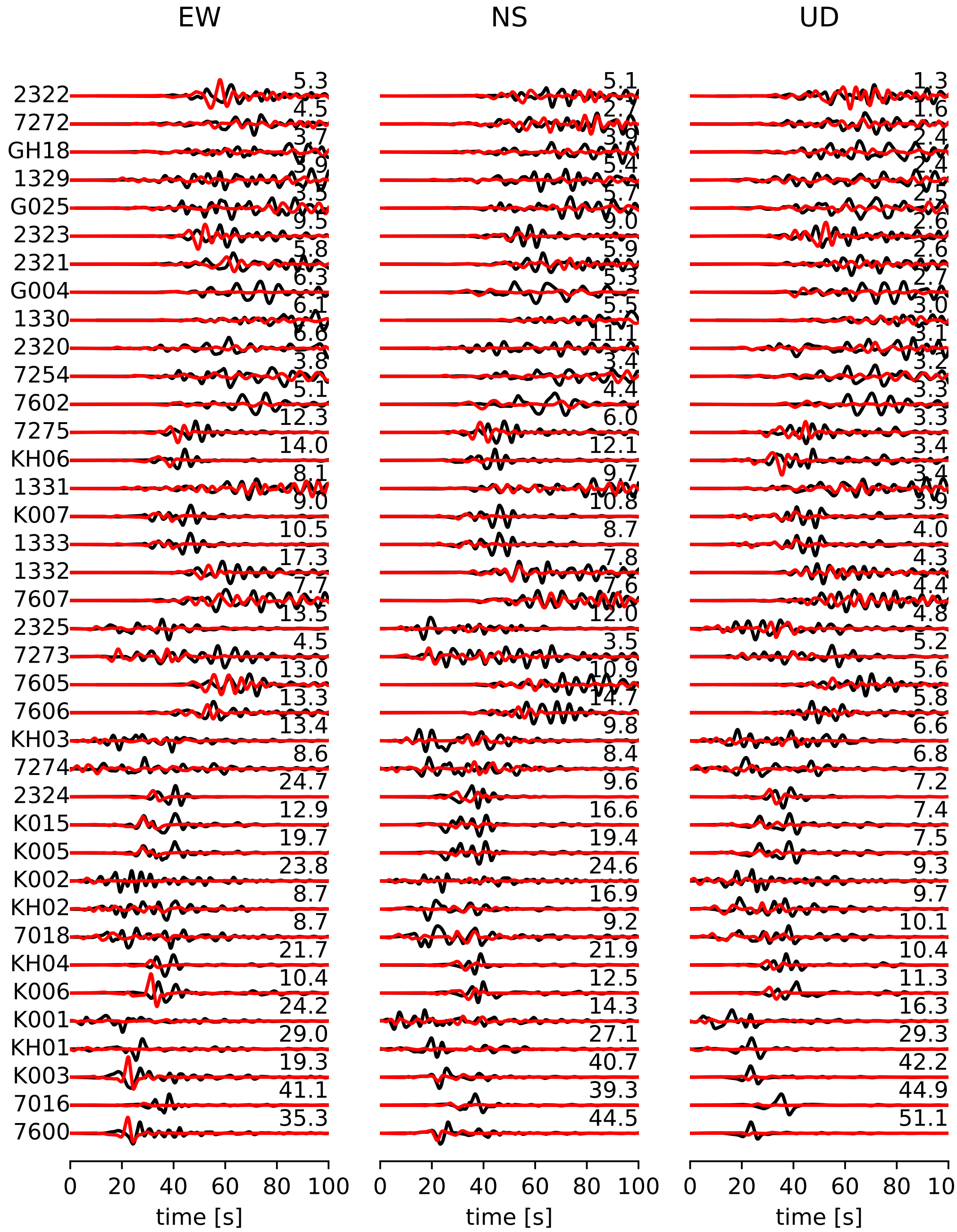

Figure S4. Comparison of observed (black lines) and synthetic (red lines) velocity waveforms at each station, with synthetic waveforms generated using the USGS finite fault model. All waveforms are filtered to a period range of 4 − 20 s and normalized by the maximum amplitude of the observed waveform for each station (indicated on the right side of each waveform). The normalization factor is in units of cm/s. Time zero corresponds to the origin time of the USGS source model (07:10:09.0 UTC).

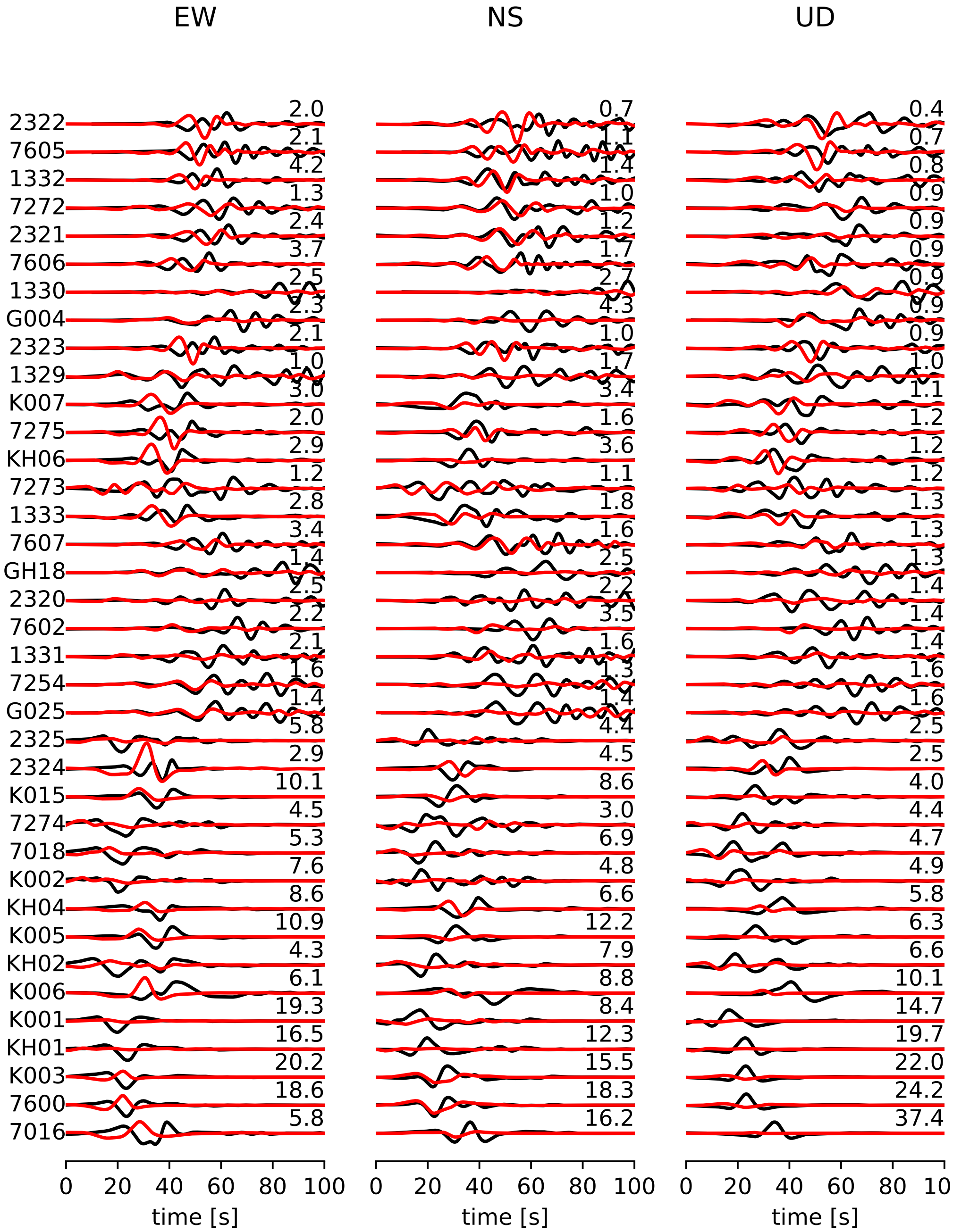

Figure S5. Comparison of observed (black lines) and synthetic (red lines) velocity waveforms at each station, with synthetic waveforms generated using the USGS finite fault model. All waveforms are filtered to a period range of 10 − 50 s and normalized to the maximum amplitude of the observed waveform for each station (indicated on the right side of each waveform). The normalization factor is expressed in cm/s. Time zero corresponds to the origin time of the USGS source model (07:10:09.0 UTC).

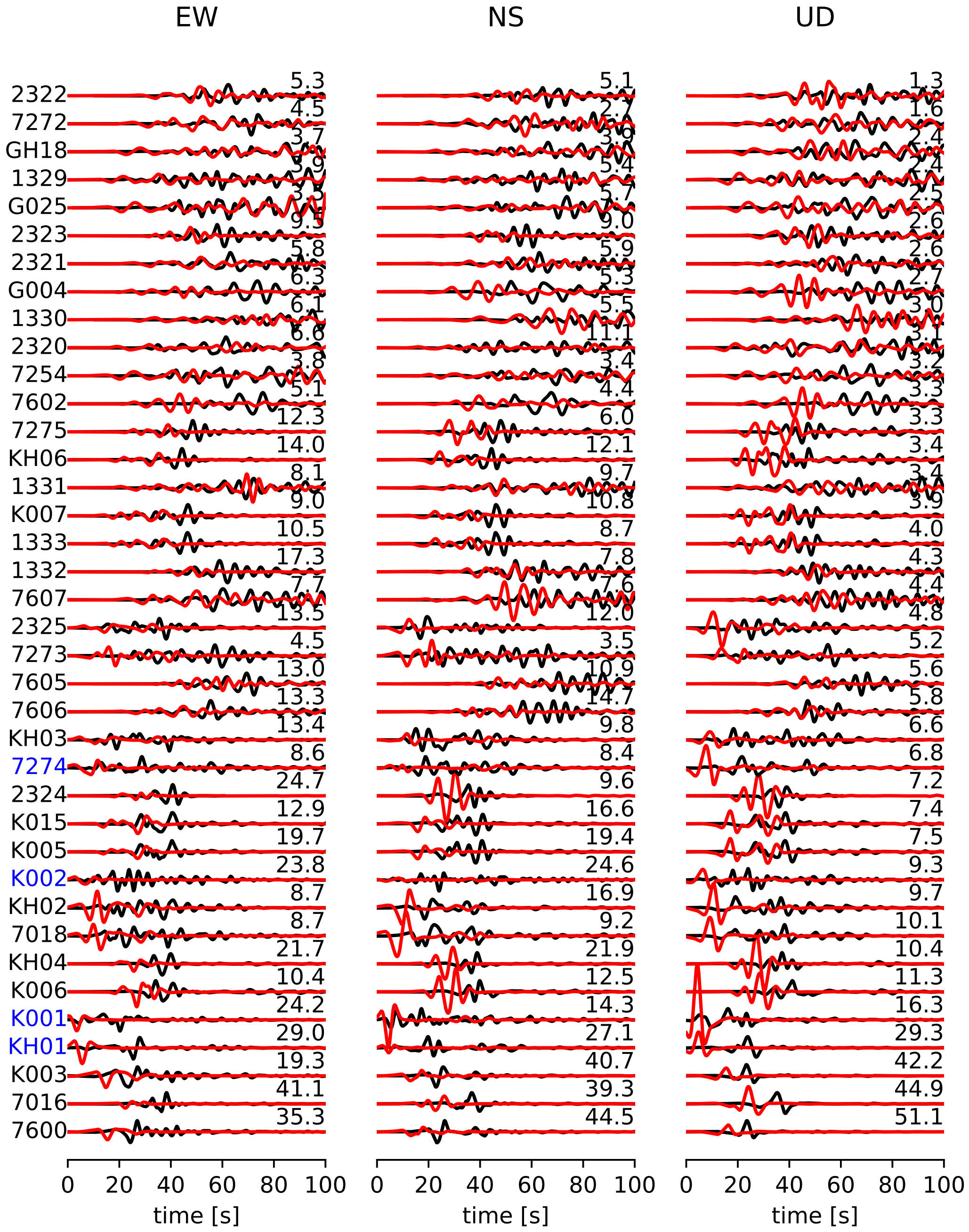

Figure S6. Comparison of observed (black lines) and synthetic (red lines) velocity waveforms at each station, with synthetic waveforms generated using our developed finite fault model with a simple-rupture scenario assuming a constant $V_r = 2.0$ km. All waveforms are filtered to a period range of 4 – 20 s and normalized to the maximum amplitude of the observed waveform for each station (indicated on the right side of each waveform). The normalization factor is given in cm/s. Observed waveforms at stations in the epicentral region, such as K001 and 7274 (highlighted in green), exhibit two or more main phase arrivals separated by several seconds or more. Time zero corresponds to the origin time assumed in this study (07:10:09.5 UTC).

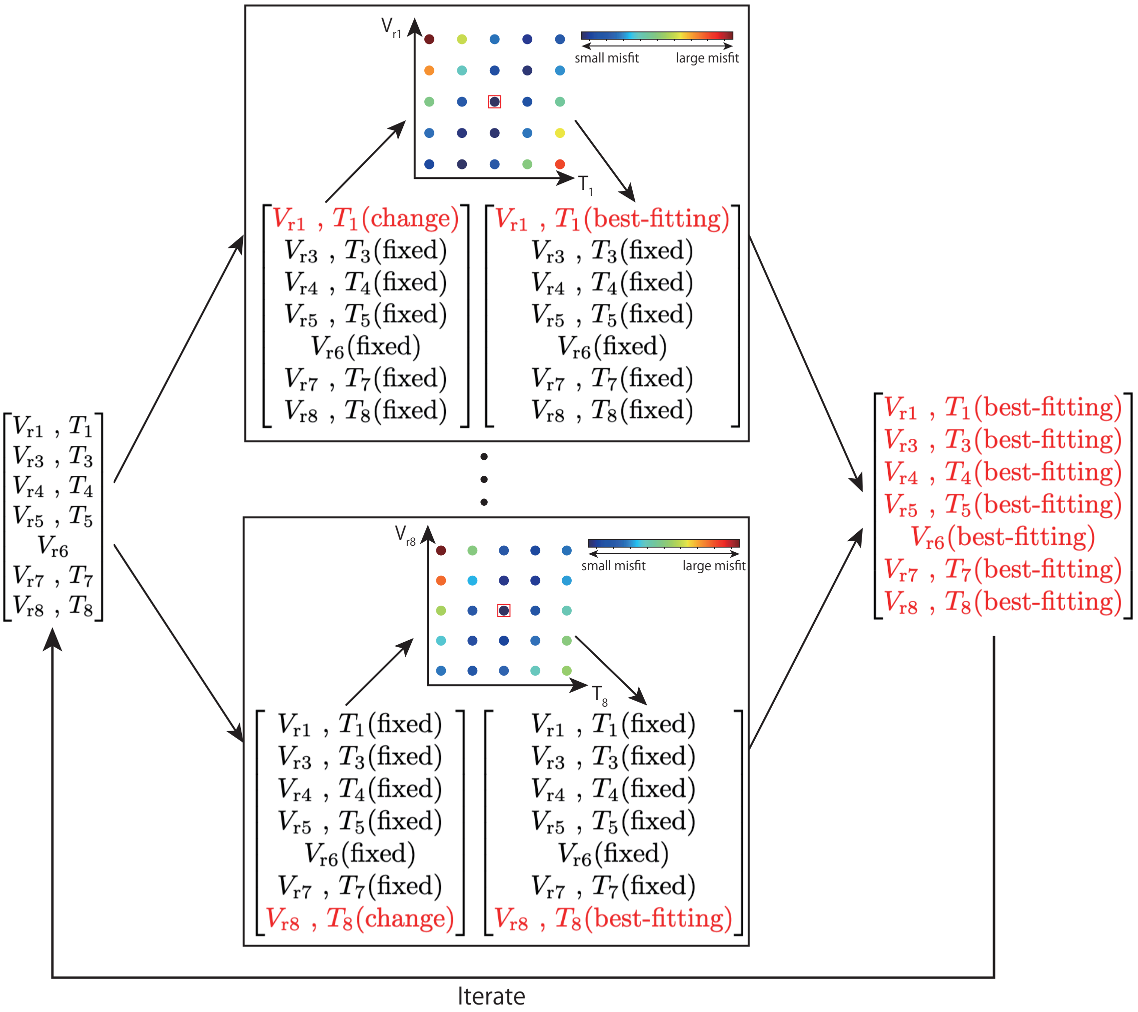

Figure S7. A schematic diagram illustrating the overall parameter exploration procedure.

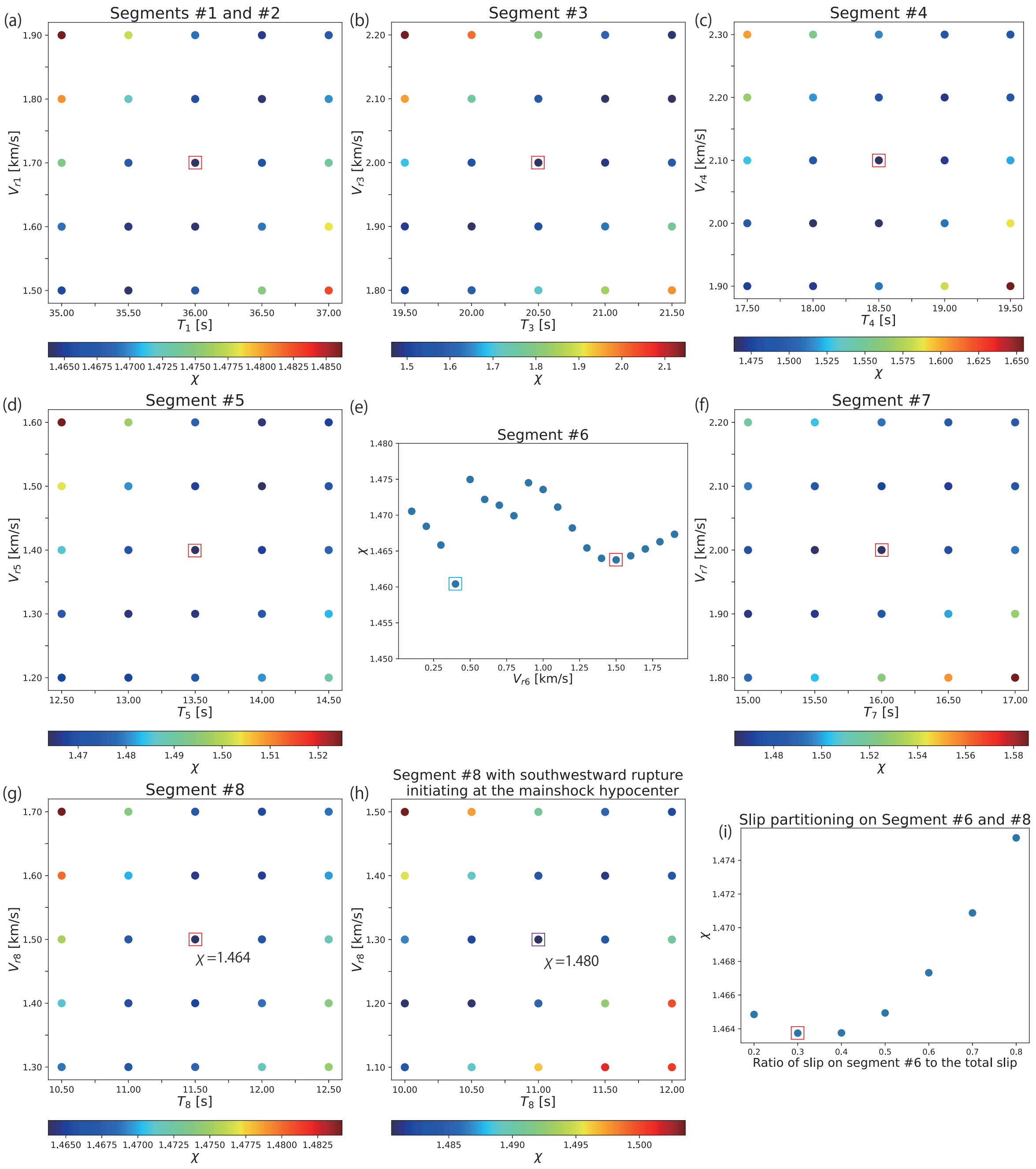

Figure S8. Results of the parameter exploration conducted during the final iteration of the grid search procedure shown in Figure S7. (a-h) A grid search is conducted for 16 parameters: V_r shown in each subplot and the corresponding rupture initiation times (e.g., T_1, T_3, etc.), excluding the origin time. Each parameter is adjusted to minimize the χ value. Open red squares in each subplot indicate the best-fitting parameter for each fault segment, corresponding to the smallest misfit value except for Segment #6 where the smallest misfit with $V_{\mathrm{r}4} = 0.4$ km/s (blue square). The purple square shows the smallest misfit among the cases with the southwestward rupture on Segment #8. (i) A grid search to identify the optimal partition of the total slip between Segments #6 and #8.

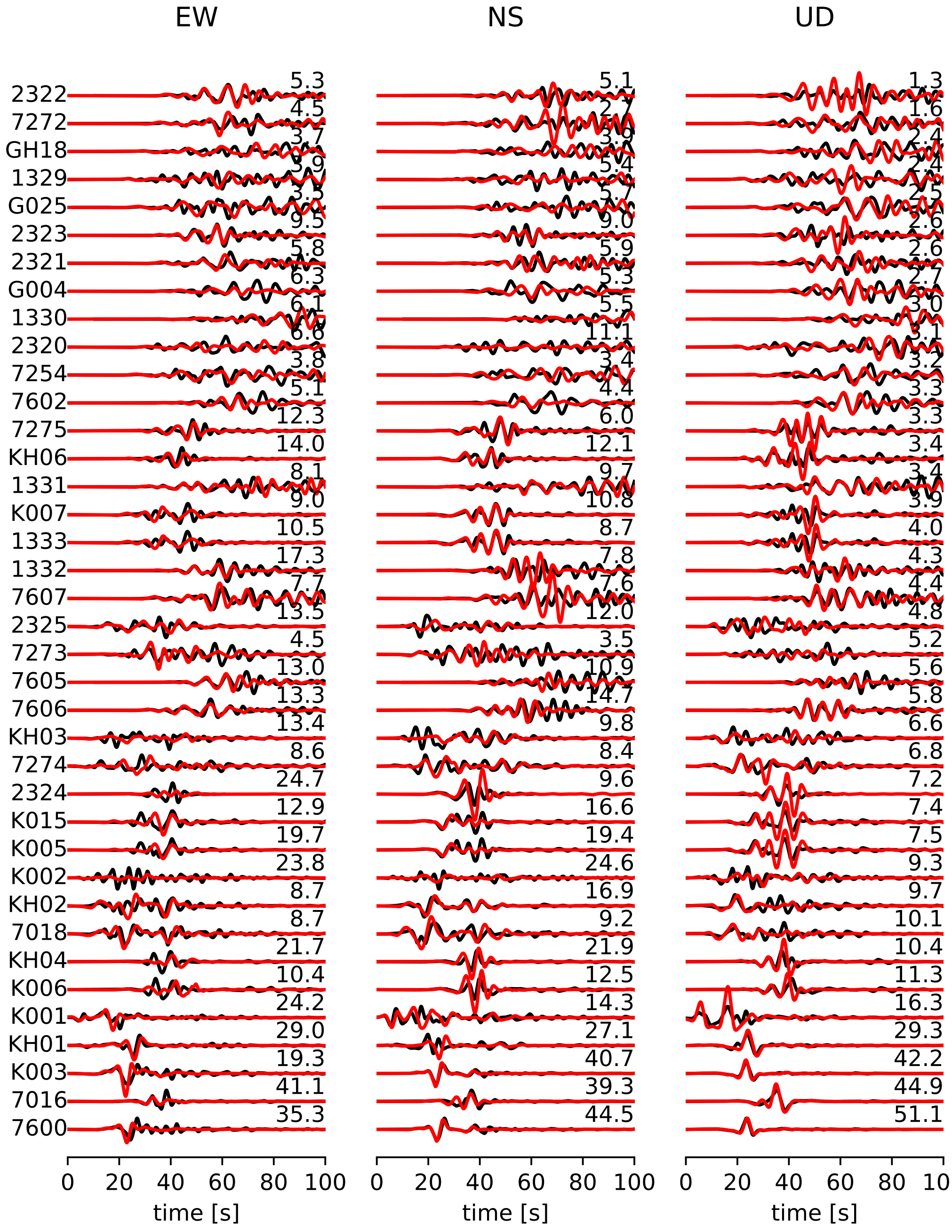

Figure S9. Comparison of observed (black lines) and synthetic (red lines) velocity waveforms at each strong-motion station, with synthetic waveforms computed using the best-fit fault model. All waveforms are bandpass-filtered to a period range of 4 – 20 s and normalized to the maximum amplitude of the observed waveforms at each station. Stations are sorted by observed peak vertical velocity, from largest (bottom) to smallest (top). The normalization factor, displayed on the right side of each waveform, is given in cm/s. Time zero corresponds to the origin time assumed in this study (07:10:09.5 UTC).

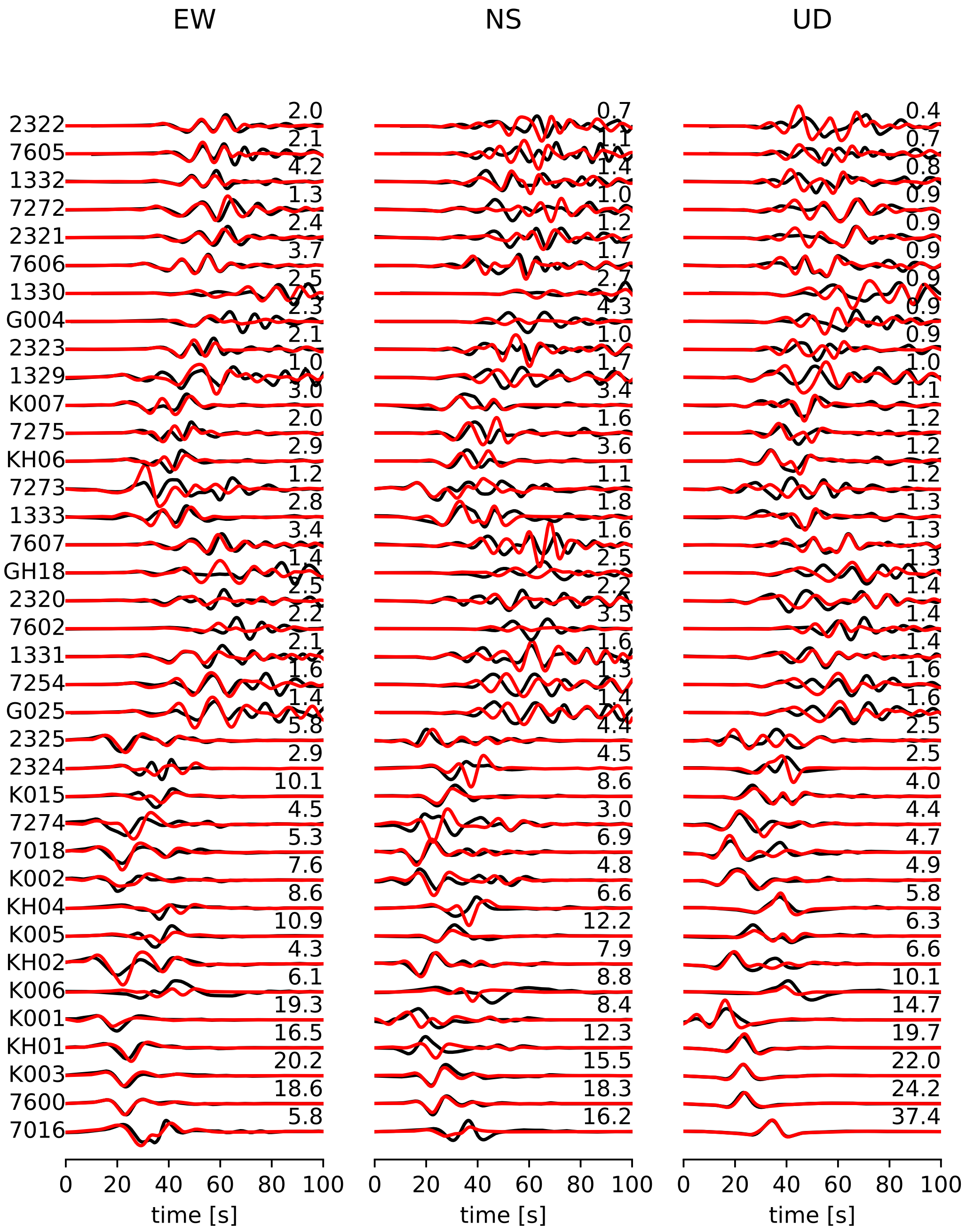

Figure S10. Comparison of observed (black lines) and synthetic (red lines) velocity waveforms at each station, computed using the best-fit fault model. All waveforms are bandpass-filtered to a period range of 10 – 50 s and normalized to the maximum amplitude of the observed waveforms at each station. The normalization factor, shown on the right side of each waveform, is expressed in units of cm/s. Time zero corresponds to the origin time assumed in this study (07:10:09.5 UTC).

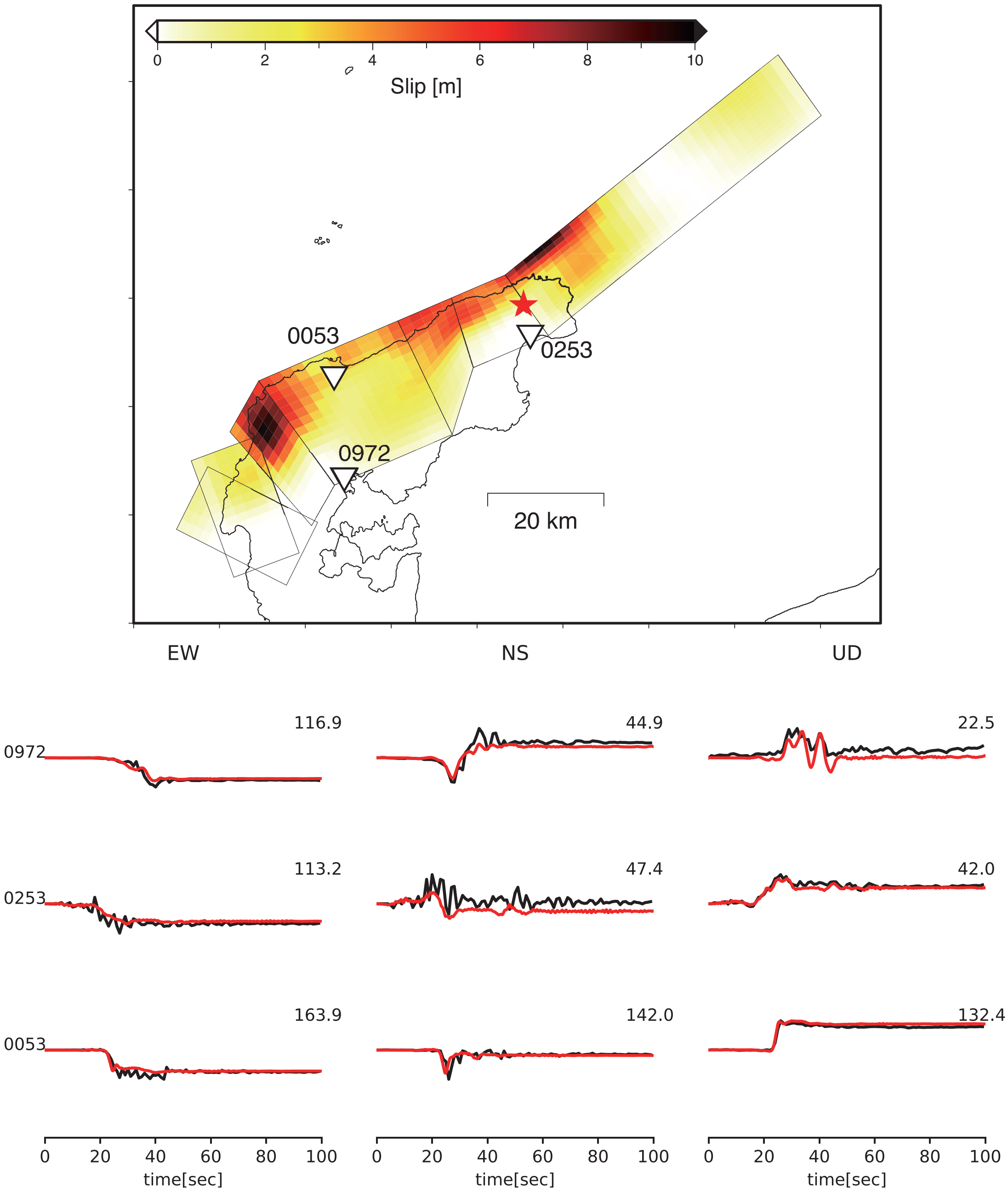

Figure S11. Comparison of observed (black lines) and synthetic (red lines) displacement waveforms at each 1-Hz GNSS station, computed using the best-fit fault model. All waveforms are normalized to the maximum amplitude of the observed waveforms at each station. The normalization factor, displayed on the right side of each waveform, is expressed in units of cm. Time zero corresponds to the origin time assumed in this study (07:10:09.5 UTC).

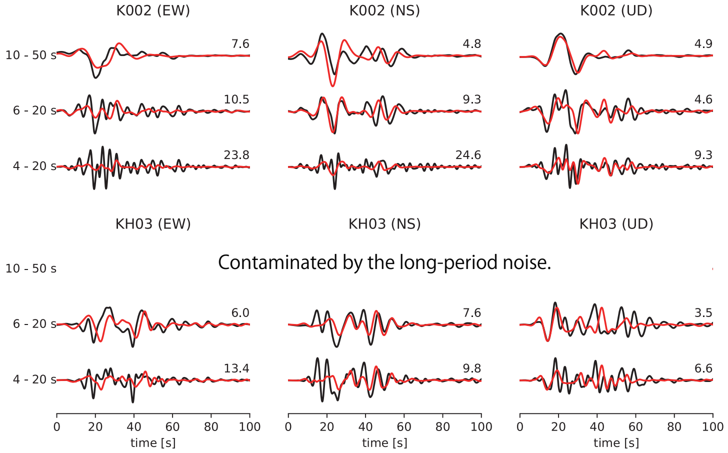

Figure S12. Comparison of observed (black lines) and synthetic (red lines) velocity waveforms at Stations K002 and KH03, with synthetic waveforms calculated from the best-fitting model. All waveforms are filtered to period ranges of 4 – 20 s, 6 – 20 s, and 10 – 50 s, and normalized by the maximum amplitude of the observed waveform at each station (normalization factor in cm/s shown on the right of each waveform). While the model does not fit shorter-period waveforms well, it provides a good fit for long-period waveforms ($\geq$6 s). Time zero corresponds to the origin time assumed in this study (07:10:09.5 UTC).

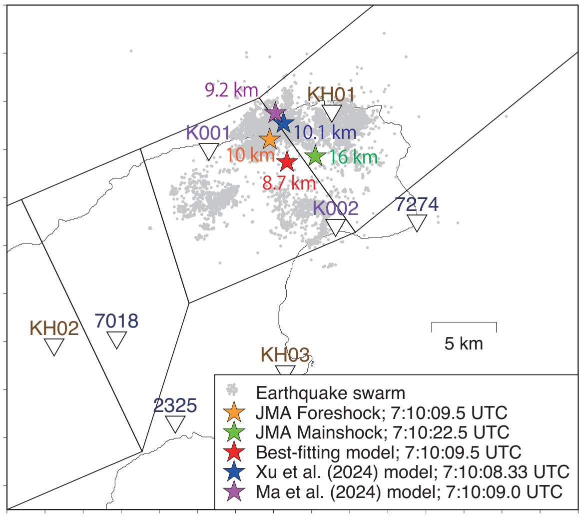

Figure S13. Map showing the epicenters of earthquake swarms, the $M_{\mathrm{jma}}5.9$ foreshock, and the $M_{\mathrm{jma}}7.6$ mainshock, along with fault models from Ma et al (2024), Xu et al (2024), and the best-fitting model. Inverted triangles indicate strong-motion stations from K-NET (purple), JMA (blue), and KiK-net (brown).

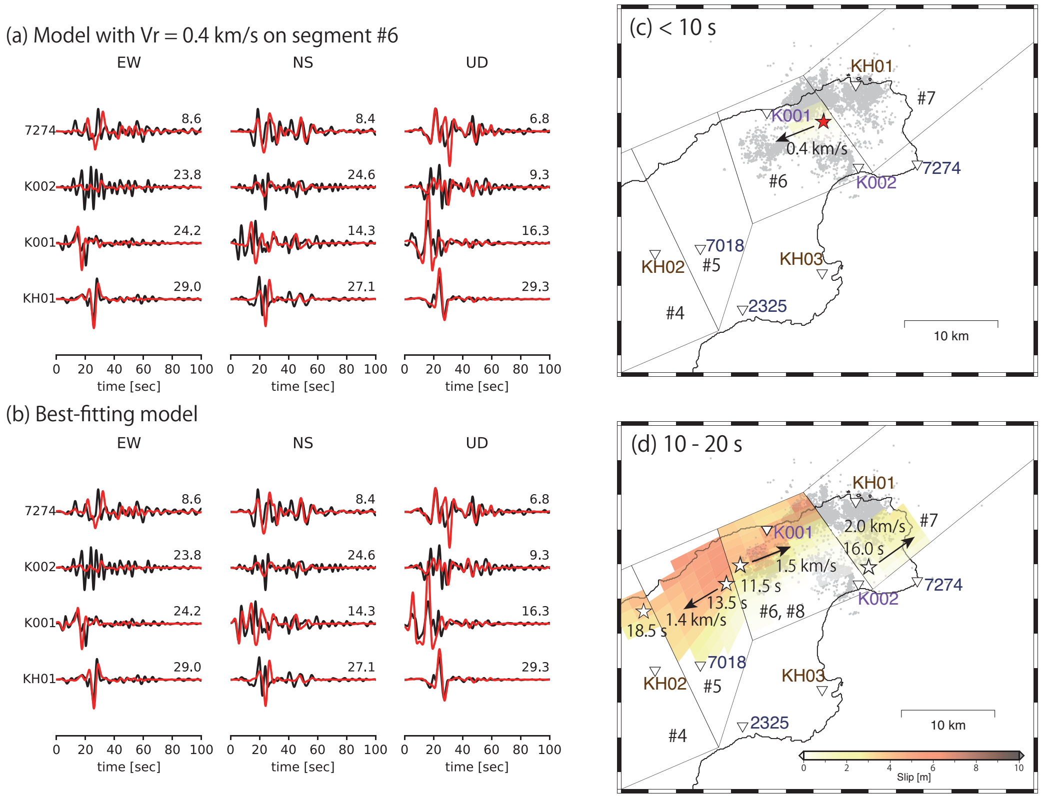

Figure S14. A source model with $V_{r6} = 0.4$ km/s (indicated by the blue square in Figure S8e). Comparison of observed (black lines) and synthetic (red lines) velocity waveforms at stations in the epicentral region for (a) the source model with $V_{r6} = 0.4$ km/s and (b) the best-fitting model. (c-d) Slip and rupture evolution in the epicentral region for the source model with $V_{r6} = 0.4$ km/s. A red star indicates the epicenter, while white stars denote the rupture initiation points for individual fault segments. Arrows and associated labels illustrate the along-strike direction and rupture propagation speed for each segment. Time zero corresponds to the origin time assumed in this study (07:10:09.5 UTC).

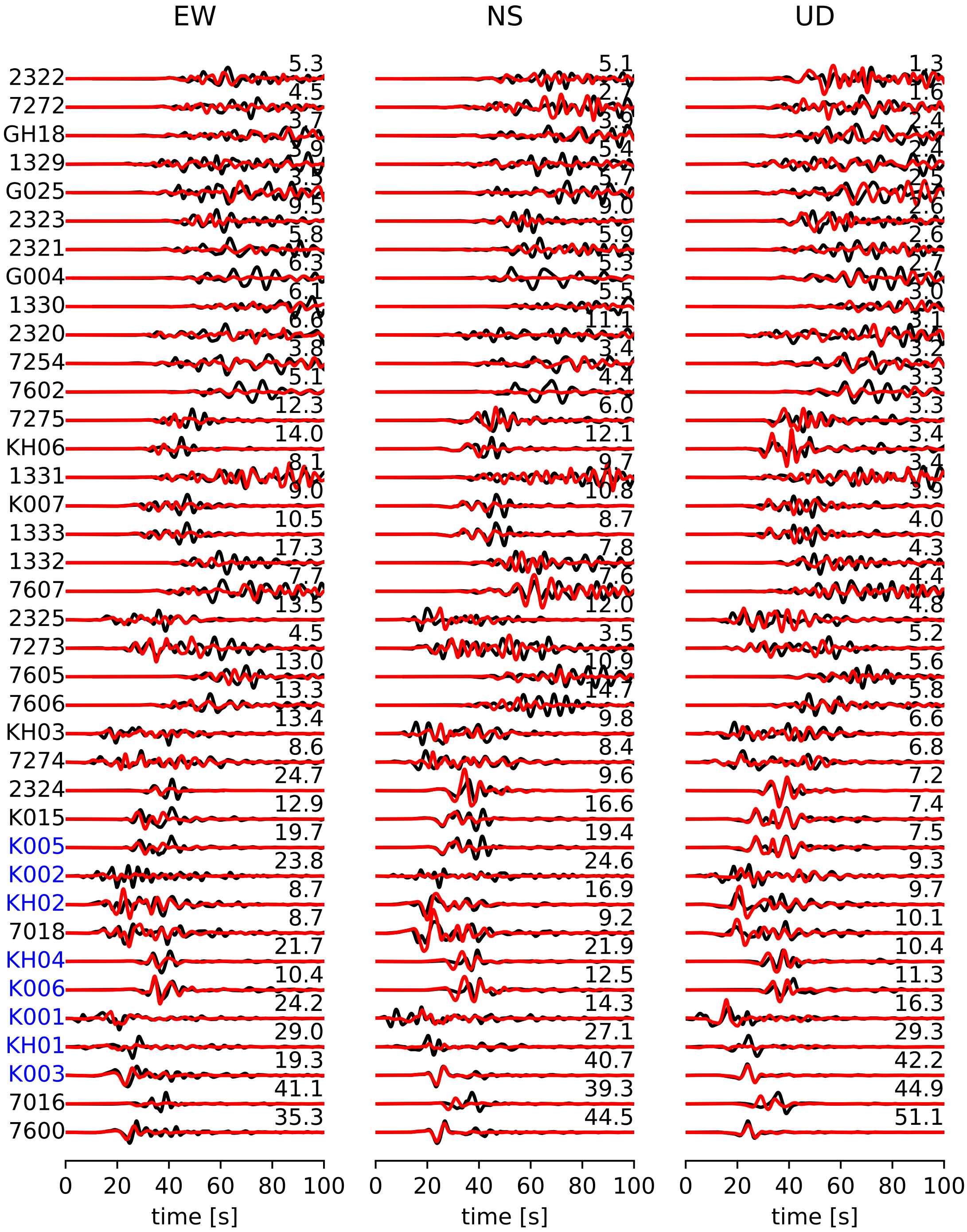

Figure S15. Comparison of observed (black lines) and synthetic (red lines) velocity waveforms at each station, computed using the Ma et al (2024) source model. Stations in blue indicate those used in the finite fault inversion by Ma et al (2024). All waveforms are bandpass-filtered to a period range of 4 – 20 s and normalized to the maximum amplitude of the observed waveforms at each station (normalization factor in cm/s shown on the right of each waveform). Time zero corresponds to 07:10:09.0 UTC.

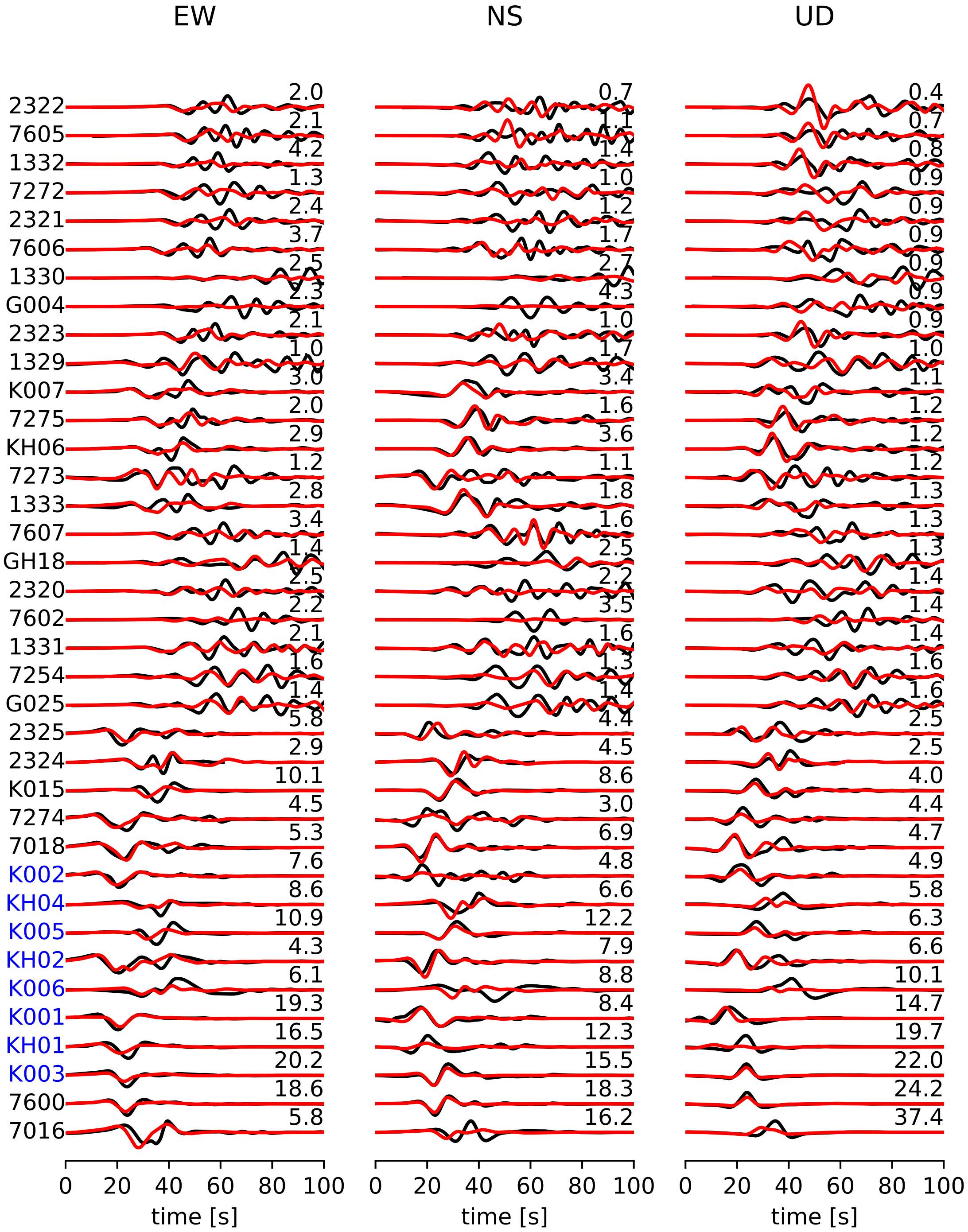

Figure S16. Comparison of observed (black lines) and synthetic (red lines) velocity waveforms at each station, computed using the Ma et al (2024) source model. Stations in blue indicate those used in the finite fault inversion by Ma et al (2024). All waveforms are bandpass-filtered to a period range of 10 – 50 s and normalized to the maximum amplitude of the observed waveforms at each station (normalization factor in cm/s shown on the right of each waveform). Time zero corresponds to 07:10:09.0 UTC.

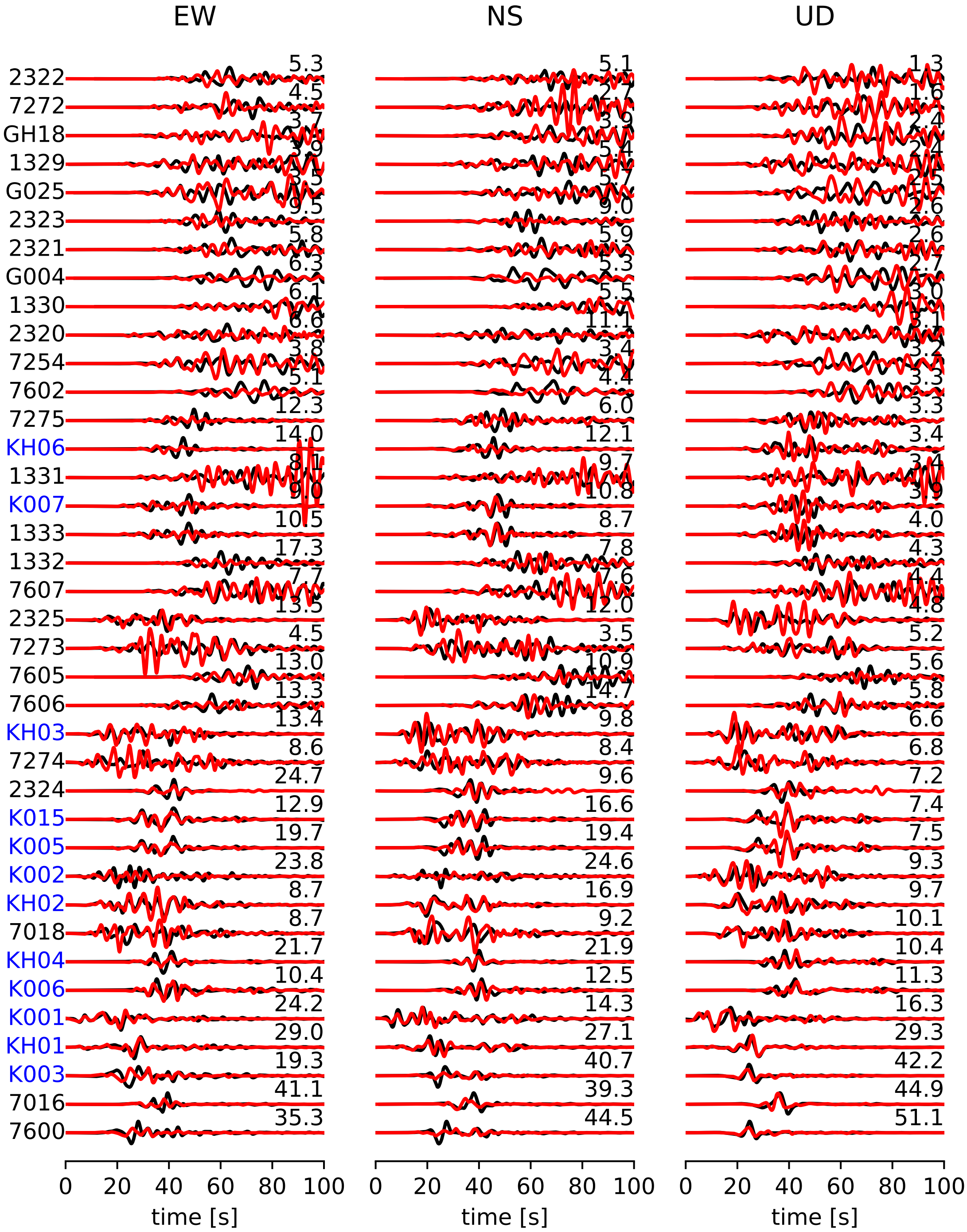

Figure S17. Comparison of observed (black lines) and synthetic (red lines) velocity waveforms at each station, computed using the Xu et al (2024) source model. Stations in blue indicate those used in the finite fault inversion by Xu et al (2024). All waveforms are bandpass-filtered to a period range of 4 – 20 s and normalized to the maximum amplitude of the observed waveforms at each station (normalization factor in cm/s shown on the right of each waveform). Time zero corresponds to 7:10:08.33 UTC.

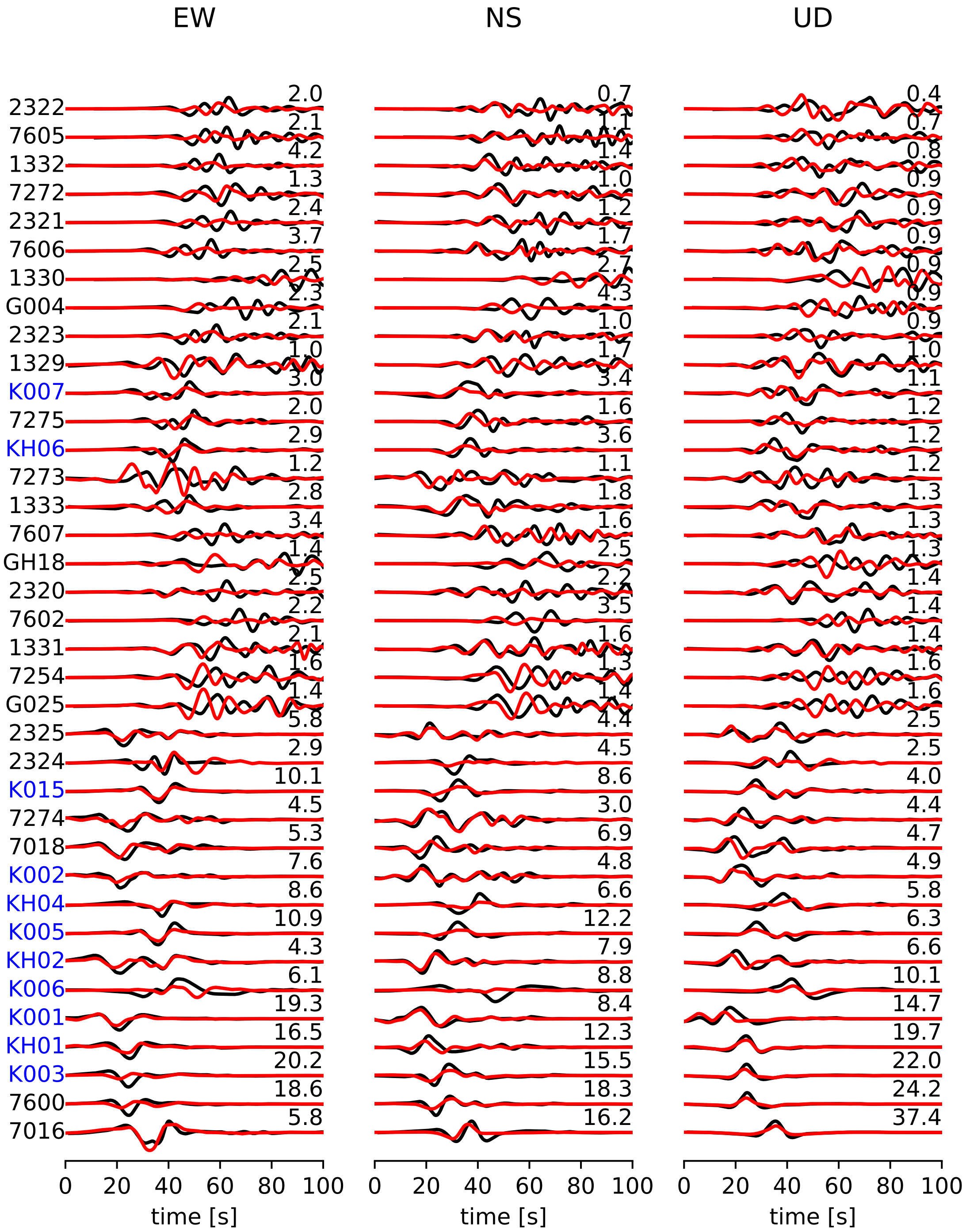

Figure S18. Comparison of observed (black lines) and synthetic (red lines) velocity waveforms at each station, computed using the Xu et al (2024) source model. Stations in blue indicate those used in the finite fault inversion by Xu et al (2024). All waveforms are bandpass-filtered to a period range of 10 – 50 s and normalized to the maximum amplitude of the observed waveforms at each station (normalization factor in cm/s shown on the right of each waveform). Time zero corresponds to 7:10:08.33 UTC.

References

Fukushima Y, Ishimura D, Takahashi N, et al (2024) Landscape changes caused by the 2024 Noto Peninsula earthquake in Japan. Science Advances 10(49):eadp9193. https://doi.org/10.1126/sciadv.adp9193

Ji C, Helmberger DV, Wald DJ, et al (2003) Slip history and dynamic implications of the 1999 Chi-Chi, Taiwan, earthquake. Journal of Geophysical Research: Solid Earth 108(B9). https://doi.org/10.1029/2002JB001764

Ma Z, Zeng H, Luo H, et al (2024) Slow rupture in a fluid-rich fault zone initiated the 2024 Mw 7.5 Noto earthquake. Science 385(6711):866–871. https://doi.org/10.1126/science.ado5143

Xu L, Ji C, Meng L, et al (2024) Dual-initiation ruptures in the 2024 Noto earthquake encircling a fault asperity at a swarm edge. Science 385(6711):871–876. https://doi.org/10.1126/science.adp0493